



LJMU Research Online

Vreeswijk, PM, Leloudas, G, Gal-Yam, A, De Cia, A, Perley, DA, Quimby, RM, Waldman, R, Sullivan, M, Yan, L, Ofek, EO, Fremling, C, Taddia, F, Sollerman, J, Valenti, S, Arcavi, I, Howell, DA, Filippenko, AV, Cenko, SB, Yaron, O, Kasliwal, MM, Cao, Y, Ben-Ami, S, Horesh, A, Rubin, A, Lunnan, R, Nugent, PE, Laher, R, Rebbapragada, UD, Woźniak, P and Kulkarni, SR

On The Early-Time Excess Emission in Hydrogen-Poor Superluminous Supernovae

<http://researchonline.ljmu.ac.uk/id/eprint/6556/>

Article

Citation (please note it is advisable to refer to the publisher's version if you intend to cite from this work)

Vreeswijk, PM, Leloudas, G, Gal-Yam, A, De Cia, A, Perley, DA, Quimby, RM, Waldman, R, Sullivan, M, Yan, L, Ofek, EO, Fremling, C, Taddia, F, Sollerman, J, Valenti, S, Arcavi, I, Howell, DA, Filippenko, AV, Cenko, SB, Yaron, O, Kasliwal, MM. Cao. Y. Ben-Ami. S. Horesh. A. Rubin. A. Lunnan. R. Nugent.

LJMU has developed **LJMU Research Online** for users to access the research output of the University more effectively. Copyright © and Moral Rights for the papers on this site are retained by the individual authors and/or other copyright owners. Users may download and/or print one copy of any article(s) in LJMU Research Online to facilitate their private study or for non-commercial research. You may not engage in further distribution of the material or use it for any profit-making activities or any commercial gain.

The version presented here may differ from the published version or from the version of the record. Please see the repository URL above for details on accessing the published version and note that access may require a subscription.

<http://researchonline.ljmu.ac.uk/>

For more information please contact researchonline@ljmu.ac.uk

<http://researchonline.ljmu.ac.uk/>

ON THE EARLY-TIME EXCESS EMISSION IN HYDROGEN-POOR SUPERLUMINOUS SUPERNOVAE

PAUL M. VREESWIJK^{1,2}, GIORGOS LELOUDAS^{1,3}, AVISHAY GAL-YAM¹, ANNALISA DE CIA^{4,1}, DANIEL A. PERLEY^{3,5}, ROBERT M. QUIMBY^{6,7}, RONI WALDMAN^{8,1}, MARK SULLIVAN⁹, LIN YAN¹⁰, ERAN O. OFEK¹, CHRISTOFFER FREMLING¹¹, FRANCESCO TADDIA¹¹, JESPER SOLLERMAN¹¹, STEFANO VALENTI¹², IAIR ARCAVI^{13,14,15}, D. ANDREW HOWELL^{14,13}, ALEXEI V. FILIPPENKO¹⁶, S. BRADLEY CENKO^{17,18}, OFER YARON¹, MANSI M. KASLIWAL⁵, YI CAO⁵, SAGI BEN-AMI^{19,1}, ASSAF HORESH¹, ADAM RUBIN¹, RAGNHILD LUNNAN⁵, PETER E. NUGENT^{20,18}, RUSS LAHER²¹, UMAA D. REBBAPRAGADA²², PRZEMYSŁAW WOŹNIAK²³, AND SHRINIVAS R. KULKARNI⁵

(Received 21 September 2016; Revised 9 November 2016; Accepted 29 November 2016)

ABSTRACT

We present the light curves of the hydrogen-poor superluminous supernovae (SLSNe-I) PTF 12dam and iPTF 13dcc, discovered by the (intermediate) Palomar Transient Factory. Both show excess emission at early times and a slowly declining light curve at late times. The early bump in PTF 12dam is very similar in duration (~ 10 days) and brightness relative to the main peak (2–3 mag fainter) compared to those observed in other SLSNe-I. In contrast, the long-duration (>30 days) early excess emission in iPTF 13dcc, whose brightness competes with that of the main peak, appears to be of a different nature. We construct bolometric light curves for both targets, and fit a variety of light-curve models to both the early bump and main peak in an attempt to understand the nature of these explosions. Even though the slope of the late-time light-curve decline in both SLSNe is suggestively close to that expected from the radioactive decay of ^{56}Ni and ^{56}Co , the amount of nickel required to power the full light curves is too large considering the estimated ejecta mass. The magnetar model including an increasing escape fraction provides a reasonable description of the PTF 12dam observations. However, neither the basic nor the double-peaked magnetar model is capable of reproducing the iPTF 13dcc light curve. A model combining a shock breakout in an extended envelope with late-time magnetar energy injection provides a reasonable fit to the iPTF 13dcc observations. Finally, we find that the light curves of both PTF 12dam and iPTF 13dcc can be adequately fit with the circumstellar medium (CSM) interaction model.

Subject headings: supernovae: general — supernovae: individual: (PTF 12dam, iPTF 13dcc)

¹ Department of Particle Physics and Astrophysics, Weizmann Institute of Science, Rehovot 7610001, Israel

² Benozziyo Fellow; email: paul.vreeswijk@weizmann.ac.il

³ Dark Cosmology Centre, Niels Bohr Institute, University of Copenhagen, Juliane Maries Vej 30, 2100 København Ø, Denmark

⁴ European Southern Observatory, Karl-Schwarzschild-Strasse 2, 85748 Garching bei München, Germany

⁵ Cahill Center for Astrophysics, California Institute of Technology, Pasadena, CA 91125, USA

⁶ Department of Astronomy, San Diego State University, San Diego, CA 92182, USA

⁷ Kavli IPMU (WPI), UTIAS, The University of Tokyo, Kashiwa, Chiba 277-8583, Japan

⁸ Racah Institute of Physics, The Hebrew University, Jerusalem 91904, Israel

⁹ School of Physics and Astronomy, University of Southampton, Southampton SO17 1BJ, UK

¹⁰ Infrared Processing and Analysis Center, California Institute of Technology, Pasadena, CA 91125, USA

¹¹ The Oskar Klein Centre, Department of Astronomy, Stockholm University, AlbaNova, 10691 Stockholm, Sweden

¹² Department of Physics, University of California, Davis, CA 95616, USA

¹³ Department of Physics, University of California, Santa Barbara, CA 93106, USA

¹⁴ Las Cumbres Observatory Global Telescope, 6740 Cortona Dr., Suite 102, Goleta, CA 93111, USA

¹⁵ Einstein Fellow

¹⁶ Department of Astronomy, University of California, Berkeley, CA 94720-3411, USA

¹⁷ Astrophysics Science Division, NASA Goddard Space Flight Center, Mail Code 661, Greenbelt, MD, 20771, USA

¹⁸ Joint Space-Science Institute, University of Maryland, College Park, MD 20742, USA

¹⁹ Smithsonian Astrophysical Observatory, Harvard-Smithsonian Center for Astrophysics, 60 Garden St., Cambridge,

MA 02138, USA

²⁰ Computational Cosmology Center, Lawrence Berkeley National Laboratory, 1 Cyclotron Road, Berkeley, CA 94720, USA

²¹ Spitzer Science Center, MS 314-6, California Institute of Technology, Pasadena, CA 91125, USA

²² Jet Propulsion Laboratory, California Institute of Technology, Pasadena, CA 91109, USA

²³ Los Alamos National Laboratory, MS D436, Los Alamos, NM 87545, USA

1. INTRODUCTION

Supernovae that reach an absolute magnitude brighter than the (arbitrary) limit of $M = -21$ are labelled superluminous (Gal-Yam 2012). Even though they are very rare, several tens of them have been discovered over the past decade thanks to the ever-increasing survey speed of optical telescopes. They are observationally separated into two classes based on the detection of hydrogen in their spectra, similar to classical supernovae (see Filippenko 1997): hydrogen-rich Type II SLSNe show clear Balmer features (e.g., Ofek et al. 2007; Smith et al. 2007), while the hydrogen-poor Type I SLSNe do not (Gal-Yam 2012). The latter commonly exhibit a distinct W-shaped feature identified as O II at rest-frame wavelengths 4000–4500 Å (Quimby et al. 2011; Mazzali et al. 2016). At late times, the spectra of these SLSNe-I evolve to appear like those of normal Type Ic SNe (Pastorello et al. 2010), leading many authors to refer to this class as SLSN-Ic. Sometimes this Type I/II distinction is not so obvious; for example, spectra of CSS121015:004244+132827 (hereafter referred to as CSS 121015) have similarities to both Type II and I objects (Benetti et al. 2014), while iPTF 13ehe, classified as Type I, shows the emergence of broad H α emission at late times (Yan et al. 2015; see also Moriya et al. 2015; Wang et al. 2016).

There is some evidence that the energy source powering the hydrogen-rich SLSNe is interaction of the SN ejecta with optically-thick material at a large distance ($\sim 10^{15}$ cm), as they typically reveal Balmer emission lines indicative of interaction with a hydrogen-rich circumstellar medium (CSM; e.g., Chevalier & Fransson 1994; Chugai & Danziger 1994; Ofek et al. 2014). Because of the similarity with normal SNe of Type IIn, this class is also referred to as SLSNe-IIn. However, some SLSNe-II do not exhibit narrow emission lines, while they are of Type II as they reveal broad hydrogen features during the photospheric phase (Inserra et al. 2016; see also Moriya & Tominaga 2012).

The energy source of the hydrogen-poor SLSNe is still under debate, with the most promising candidates being (1) additional energy input from a central engine, such as a spinning-down magnetar (e.g., Kasen & Bildsten 2010; Woosley 2010; Inserra et al. 2013) or an accreting black hole (Dexter & Kasen 2013); (2) interaction of the ejecta with a hydrogen-poor shell expelled by the progenitor star some time before the explosion (Blinnikov & Sorokina 2010; Chevalier & Irwin 2011); and (3) the radioactive decay of a large amount of nickel produced in the explosion, potentially due to pair-instability conditions (see Gal-Yam et al. 2009) though this is still being debated (Moriya et al. 2010; Young et al. 2010; Nicholl et al. 2013). The light curves of some hydrogen-poor SLSNe, such as the two PTF sources presented in this paper, decay very slowly at late times, with a slope similar to that expected from the decay of radioactive nickel and cobalt. These SLSNe are part of the hydrogen-poor class, but are sometimes referred to as Type R (“radioactive”; see Gal-Yam 2012).

The host galaxies of SLSNe are found to be irregular, compact, low-mass galaxies with high specific star formation rates (Neill et al. 2011; Lunnan et al. 2014, 2015; Leloudas et al. 2015). A comprehensive study of 32 host galaxies of all PTF-discovered SLSNe (until the

end of 2012) found hydrogen-poor SLSNe to have a preference for environments in hosts with a metallicity upper bound of about half solar, while the hydrogen-rich SLSNe do not show such a preference (Perley et al. 2016). A very similar conclusion was reached independently by Chen et al. (2016). In emission, the galaxies hosting SLSNe have broadly similar characteristics as the hosts of gamma-ray bursts (GRBs). Leloudas et al. (2015) find the host-galaxy emission-line strengths of redshift $z < 1$ SLSNe-I to be significantly stronger than in GRB hosts, but Japelj et al. (2016) do not confirm this result over the range $0.3 < z < 0.7$. In *absorption*, the environments of SLSNe-I appear to be significantly poorer in their neutral gas content, as traced by Mg I and Mg II, than those of GRBs (Vreeswijk et al. 2014).

Focusing on the hydrogen-poor class, several of these have shown evidence for an early-time light-curve “bump” or excess emission before the onset of the main peak. Examples are SN 2006oz (Leloudas et al. 2012), LSQ 14bdq (Nicholl et al. 2015), and DES 14X3taz (Smith et al. 2016). In fact, Nicholl & Smartt (2016) suggest that early bumps such as the ones above may be ubiquitous in hydrogen-poor SLSNe. Early bumps have also been observed in normal stripped-envelope SNe, and recently in a normal SN Ic from a massive progenitor (Taddia et al. 2016). To date, such early excess emission has not been reported for any hydrogen-rich SLSN-II. This early excess emission is of particular interest, as it may provide a clue regarding what is powering these explosions.

In the case of SN 2006oz, Leloudas et al. (2012) propose that the precursor bolometric plateau might be related to a recombination wave in a H-poor CSM. The study by Moriya & Maeda (2012) has shown that a dip in the light curve is naturally expected when shock breakout occurs within a dense CSM. Nicholl et al. (2015) propose that the initial peak in LSQ 14bdq may arise from the post-shock cooling of extended stellar material, while reheating by a central engine is driving the main peak. The high kinetic energy inferred from fitting the Rabinak & Waxman (2011) model to the initial peak ($E_k \sim 2 \times 10^{52}$ erg) of LSQ 14bdq may favor a black hole accretion engine (Dexter & Kasen 2013) rather than a magnetar. The early-time excess emission in the case of DES 14X3taz shows rapid cooling from 22,000 K to 8,000 K over the course of 15 rest-frame days. The authors find that a shock-cooling model of CSM at a distance of $\sim 400 R_\odot$, followed by a magnetar causing the main peak of the light curve can adequately explain the entire light curve.

In this paper, we present two SLSNe-I discovered by the (intermediate) Palomar Transient Factory (Rau et al. 2009; Law et al. 2009) that also show evidence for early excess emission: PTF 12dam and iPTF 13dcc. The modest bump in PTF 12dam is very similar in duration and brightness relative to the main peak to the cases discussed above. However, the long-duration early excess emission in iPTF 13dcc, whose brightness competes with that of the main peak, appears to be of a different nature.

This paper is organized as follows. In Sec. 2 we present the photometric observations that we obtained for PTF 12dam and iPTF 13dcc, as well as the spectroscopic sequence of iPTF 13dcc. We construct the bolo-

Table 1
Log of Spectroscopic Observations of iPTF 13dcc

UTC Date	Telescope	Instrument	Exp. Time (min.)	Grating/Grism/Filter	Slit Width "	λ Coverage (Å)	Res. ^a (Å)	I.Q. ^b "	Airm.
2013 Nov. 26	P200	DBSP	20	600/4000, 316/7500	1.5	3400–10,400	9.3	2.9	1.3
2013 Dec. 3	Keck I	LRIS	21	400/3400, 400/8500	1.0	3200–10,240	6.0	1.6	1.4
2013 Dec. 4	Keck I	LRIS	10	600/4000, 400/8500	1.0	3140–10,240	5.8	1.2	1.4
2013 Dec. 31	Magellan Baade	IMACS	25	Gra-300-4.3	0.9	3700–9,700	6.1	0.9	1.3
2014 Jan. 6	P200	DBSP	60	600/4000, 316/7500	1.5	3300–10,400	8.5	1.8	1.6

^a The resolution of the spectra was determined from the width of the [O I] λ 5577 night-sky line.

^b The image quality, or effective seeing, was measured directly from the width of the object’s spatial profile around 6000 Å.

metric luminosity evolutions in Sec. 3, which we confront with models in Sec. 4. The models (see Chatzopoulos et al. 2012, 2013; Piro 2015) assume different energy sources (radioactive decay, magnetar heating, and CSM interaction) and predict the ensuing light curve based on a number of parameters; we infer estimates of the best-fit values by fitting the semi-analytical models to the bolometric light curves. We discuss our results and briefly conclude in Sec. 5.

Unless noted otherwise, the uncertainties listed in this paper are at the 1σ confidence level. We adopt the cosmological parameters as derived by the Planck collaboration in 2015 ($H_0 = 68 \text{ km s}^{-1} \text{ Mpc}^{-1}$, $\Omega_m = 0.31$, $\Omega_\Lambda = 0.69$; Planck Collaboration et al. 2016).

2. IDENTIFICATION, OBSERVATIONS, AND DATA REDUCTION

2.1. PTF 12dam

PTF 12dam was flagged as a transient source as part of the regular PTF operations on 2012 April 17 (UTC dates are used throughout this paper); it was first detected on April 10. The source is located at $\alpha = 14^{\text{h}}24^{\text{m}}46.20^{\text{s}}$, $\delta = +46^{\circ}13'48.3''$ (J2000.0), with an uncertainty of $0.1''$. At this location the Galactic extinction is estimated to be low, $A_V = 0.033 \text{ mag}$ (Schlafly & Finkbeiner 2011; see also Cardelli et al. 1989). Spectroscopic follow-up observations were performed with the Kast Spectrograph (Miller & Stone 1993) at the Lick 3 m Shane telescope, and the Low Resolution Imaging Spectrograph (LRIS; Oke et al. 1995) at the Keck I 10 m telescope (on Mauna Kea, Hawaii) on 2012 May 20, 21, and 22, showing PTF 12dam to be an SLSN-I at $z = 0.107$ (Quimby et al. 2012). The full PTF 12dam spectroscopic sequence will be presented by Quimby et al. (in prep.).

PTF 12dam was imaged with the Palomar Oschin 48 inch (P48) (i)PTF survey telescope equipped with a $12\text{k} \times 8\text{k}$ CCD mosaic camera (Rahmer et al. 2008) in the Mould R filter, the Palomar 60 inch (P60) and CCD camera (Cenko et al. 2006) in Johnson B and Sloan Digital Sky Survey (SDSS) gri , the Las Cumbres Observatory Global Telescope Network (LCOGT; Brown et al. 2013) in SDSS r , with LRIS mounted on the Keck I telescope in R_s . Post-peak and late-time imaging shows PTF 12dam to have a slowly declining light curve, i.e., of Type R following the SLSN classification suggested by Gal-Yam (2012).

PTF 12dam, relatively nearby at $z = 0.107$, has already received considerable interest in the literature. Nicholl et al. (2013) use its light curve to argue against the claim that SN 2007bi, also an SLSN-R with a similar late-time light curve as PTF 12dam, is produced by

a pair-instability explosion (Gal-Yam et al. 2009). Chen et al. (2015) study both the late-time SN decay and the host galaxy of PTF 12dam. They find that its light curve can be fit with a magnetar model (see Kasen & Bildsten 2010; Woosley 2010) if an escape fraction, increasing with time, of the magnetar energy input is considered (see also Wang et al. 2015). An even better fit is reached with a model involving the interaction of the ejecta with dense CSM. Using radiation-hydrodynamics calculations, Baklanov et al. (2015) show that PTF12dam and similar SLSNe can be explained without a magnetar in a model with a radiative shock in a dense circumstellar envelope. The host galaxy of PTF 12dam is a compact, low-mass ($3 \times 10^8 M_\odot$), low-metallicity ($12 + \log[\text{O}/\text{H}] = 8.05 \pm 0.09$) dwarf galaxy with a high star-formation rate ($5 M_\odot \text{ yr}^{-1}$; Chen et al. 2015). Thöne et al. (2015) report on long-slit spectroscopy of the host to infer the presence of a very young stellar population (even down to about 3 Myr).

2.2. iPTF 13dcc

iPTF 13dcc has not had any exposure in the literature yet. It was flagged as a transient source on 2013 August 29, which is the day that it was also first detected, with a magnitude of $r \approx 19.7$. It was initially slowly fading, but it surprisingly rebrightened by almost a magnitude, tens of days after discovery. iPTF had not observed this field before this date for almost a year (2012 September 28). The Catalina Sky Survey (CSS; Drake et al. 2009) monitored this field in early January 2013²⁴, but there are no additional detections or useful limits during the months preceding the date of discovery. The images of the iPTF 13dcc field from the 2010 and 2012 PTF observing campaigns only show upper limits at the iPTF 13dcc location. Its sky coordinates are $\alpha = 2^{\text{h}}57^{\text{m}}02.50^{\text{s}}$, $\delta = -00^{\circ}18'44.0''$ (J2000.0), with an uncertainty of $0.1''$. It was independently discovered by the Catalina Real Time Survey (CRTS) on 2013 September 12 and given the name CSS130912:025702–001844 (Drake et al. 2013). At this location the Galactic extinction is estimated to be moderate, $A_V = 0.18 \text{ mag}$ (Schlafly & Finkbeiner 2011; Cardelli et al. 1989). Spectroscopic follow-up observations were performed with the Double Spectrograph (DBSP) at the Palomar 200 inch (P200), LRIS at Keck I, and the Inamori-Magellan Areal Camera & Spectrograph (IMACS) at the Magellan *Baade* telescope, showing iPTF 13dcc to be a SLSN at $z = 0.4305$.

iPTF 13dcc was imaged with the P48 Oschin (i)PTF survey telescope in the Mould R filter, the P60 in SDSS

²⁴ see <http://nessi.cacr.caltech.edu/DataRelease>

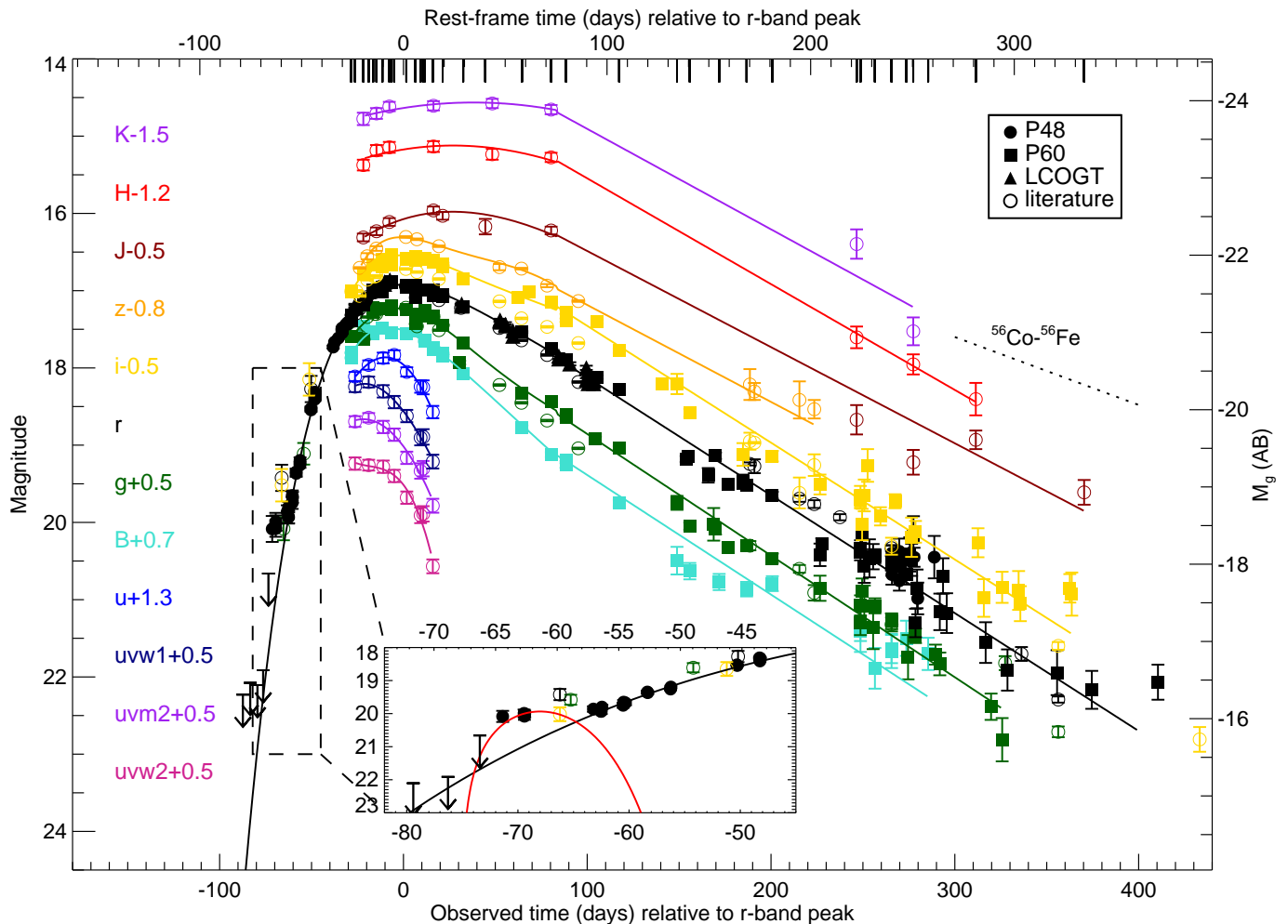


Figure 1. Light curves of PTF 12dam. Different colors and symbols denote different filters and telescopes, respectively. The solid lines show polynomial fits to the data points, where the early-time data (before $t_{\text{obs}} = 80$ days) are fit with a polynomial of order 2–5, while the late-time data are fit with a straight line. The inset displays a zoom of the very early-time light curve, showing evidence for an initial plateau with a duration of about 5–10 days. The solid red line in the inset shows a fit to the early-time r -band light curve using the Piro (2015) model, explained in more detail in Sec. 4. The late-time light curve is not that different from the decay expected from full trapping of gamma rays produced in the radioactive decay of ^{56}Co to ^{56}Fe , as indicated by the dotted line. The short vertical lines at the top show the epochs at which we constructed spectral energy distributions (SEDs) to derive the bolometric light curve. The absolute g -band AB magnitude corresponding to the observed r -band light curve around peak is indicated on the right-hand axis.

gri , the 4.3-m Discovery Channel Telescope (DCT, at Lowell Observatory, Arizona) with the Large Monolithic Imager (LMI) in SDSS ri , and finally with the *HST* Advanced Camera for Surveys (ACS) Wide-Field Camera using filter F625W (under program GO-13858; P.I. A. De Cia).

2.3. Data Reduction

All PTF 12dam and iPTF 13dcc images were reduced in a standard fashion; for the P48 images this was done using the IPAC pipeline (Laher et al. 2014). Image-subtraction point-spread function (PSF) photometry is performed on all P48 and P60 images using a custom routine written by one of us (M.S.). This pipeline is described by Firth et al. (2015); it constructs deep reference images – from either before the SN explosion or after the SN has faded – and astrometrically aligns the images using the Automated Astrometry described by Hogg et al. (2008) and the Naval Observatory Merged Astrometric Dataset (NOMAD; Zacharias et al. 2004). The image PSFs are matched in order to perform im-

age subtraction, and PSF photometry is extracted from the difference image at the SN location. The fluxes are calibrated against the SDSS Data Release 10 (Ahn et al. 2014) when available, and otherwise using the photometric catalog of Ofek et al. (2012). The LCOGT data have been reduced using a custom pipeline developed by one of us (S.V.). This pipeline is described in the Appendix of Valenti et al. (2016), and employs standard procedures (PYRAF, DAOPHOT) in a PYTHON framework. Host-galaxy flux was removed using image-subtraction technique HOTPANTS²⁵). PSF magnitudes were computed on the subtracted images and transformed to the standard SDSS filter system via standard-star observations taken during clear nights. The logs of the photometric observations of PTF 12dam and iPTF 13dcc are presented in Tables 10 and 11, respectively.

The iPTF 13dcc spectra were reduced using standard pipelines and will be made digitally available via WIS-

²⁵ High Order Transform of PSF ANd Template Subtraction; <http://www.astro.washington.edu/users/beckerv2.0/hotpants.html>

eREP (Yaron & Gal-Yam 2012). The log of these spectroscopic observations is given in Table 1.

3. PHOTOMETRIC EVOLUTION

3.1. PTF 12dam

Figure 1 shows the resulting light curve of PTF 12dam, combining data from our PTF campaign (filled circles, squares, and triangles for P48, P60, and LCOGT data, respectively) with measurements published in the literature (open circles) from Nicholl et al. (2013) and Chen et al. (2015), which include ultraviolet (UV) observations by *Swift* (Gehrels et al. 2004). All UV and optical filters are in the AB system (Oke & Gunn 1983), while the near-infrared (NIR) filters *JHK* are in the Vega system. The magnitudes shown have been corrected for the Galactic extinction along this sightline ($E_{B-V} = 0.01$ mag; Schlafly & Finkbeiner 2011). We performed polynomial fits to the light curves (magnitudes versus linear time) with the order ranging from two (for filters with a sparsely sampled light curve, such as *JHK*) to five (for the well-sampled *r*-band data) at phases between -60 and $+75$ days (here and throughout the paper, phase refers to the time in days relative to the main peak in the *r*-band filter in the *rest* frame). For the filters with measurements beyond $+75$ days, the data are adequately described by a straight line – that is, an exponential decay of the flux in time. The combined early- and late-time fits are shown by the solid lines. For the filters *Bgri* these fits were performed only to PTF data. The observed late-time slopes are in the range $0.012 - 0.016$ mag day $^{-1}$ for all filters. The inset shows a close-up view of the early-time light curve, which includes a Piro (2015) model fit (solid red line) discussed in Sec. 4.

The peak brightness in the observed *r* band of $m_r = 16.9$ mag is reached at a modified Julian date (MJD) of 56096.7, corresponding to UTC 2012 June 18.7. At this epoch, we determine a K-correction (see Hogg et al. 2002) from observed *r* to rest-frame SDSS *g* of -0.01 , resulting in an absolute *g*-band peak magnitude of M_g , peak = -21.6 (the distance modulus of PTF 12dam is 38.55 mag). The K_{rg} -correction is determined assuming that PTF 12dam is radiating like a blackbody, adopting the temperature evolution as inferred below (see Fig. 3). The absolute *g*-band magnitude is plotted on the right-hand axis of Fig. 1. We note that as the K-correction evolves in time (K_{rg} develops from $+0.2$ at a phase of -70 days, to -1.0 at $+334$ days), the scale on this axis is only valid for the *r*-band light curve (in black) around peak magnitude. Our earliest detections of the SN, between -60 and -55 rest-frame days before the *r*-band peak, show evidence for significant emission in excess of that expected from extrapolation of the polynomial fit – see the inset in Fig. 1. What appears to be a single data point in the light curve, at -70 days in the observer’s frame, actually consists of three independent measurements, making the excess above the polynomial fit highly significant. This excess emission is only clear from the PTF data, and has not been inferred from imaging data sets published to date (e.g., Nicholl et al. 2013). The *r*-band limiting magnitudes shown have been determined by coadding all the images (typically three) taken during a single night.

In order to derive the bolometric light curve of

PTF 12dam, we select a number of epochs at which we construct spectral energy distributions (SEDs). These correspond to the epochs at which observations were performed in the near-UV by *Swift*, the *B*- or *K*-band filters; they are indicated as short solid lines at the top of Fig. 1. We adopt the magnitude as estimated by the polynomial fits at a particular epoch, and the magnitude error from the measurement in the same filter closest in time to the SED epoch.

Two example SEDs, taken from epochs with phases -19.7 and $+10.4$ days, are shown in Fig. 2. The overall shape of the SEDs for all epochs is very similar to that of a Planck function. We first fit Planck functions to the observed SEDs (which have been corrected for Galactic extinction) by converting the observed magnitude to flux in the rest frame at the central wavelengths of the filters. These fits provide an estimate of the blackbody effective temperature (T_{bb}) and radius (R_{bb}); they are shown by the dashed lines in the example SEDs in Fig. 2. It is clear that both the near-UV and the NIR parts of the SED are poorly fit.

We account for the additional UV absorption by utilizing the spectrum of PTF 12dam as observed by *HST* on 2012 May 26, at a phase of -20 days (Quimby et al., in prep.). This spectrum is well approximated by a Planck function redward of 3000 \AA , while strong absorption features are present blueward of that. These near-UV features are at very similar wavelengths as the features observed in other SLSNe, such as SCP 06F6 (Barbary et al. 2009), SNLS 06D4eu (Howell et al. 2013), and iPTF 13ajg (Vreeswijk et al. 2014). We normalize the *HST* spectrum blueward of 3000 \AA (rest frame), so it can be used to modify the Planck function to be fit, as explained below. The flux below a rest-frame wavelength of 1800 \AA in this template spectrum is assumed to be zero, which is a fair assumption as the SLSNe with spectra down to this rest-frame wavelength show very low flux levels in that spectral region and the flux is rapidly declining toward the blue.

We again perform Planck-function fitting, but rather than converting magnitudes to rest-frame flux, we instead first construct a Planck spectrum at a distance of 10 pc in the rest frame, based on the two fit parameters T_{bb} and R_{bb} . This spectrum is then modified in the region $1800\text{--}3000 \text{ \AA}$ with the normalized *HST* spectrum (in the rest frame), by simply multiplying the *HST* and the blackbody spectra over this wavelength region. Below 1800 \AA it is assumed to be zero, beyond 3000 \AA it is a pure blackbody. This template spectrum is then converted to the observer’s frame [with the spectrum in units of $\text{erg s}^{-1} \text{ cm}^{-2} \text{ \AA}^{-1}$; the spectrum is multiplied by $(10/d_{1,\text{pc}})^2/(1+z)$, where $d_{1,\text{pc}}$ is the luminosity distance of PTF 12dam in pc], and magnitudes are extracted from this spectrum by performing synthetic photometry (using the filter transmission curves) to obtain model magnitudes for each filter. These model magnitudes are fit to the observed magnitudes to obtain the best-fit T_{bb} and R_{bb} . To allow for the absorption features in the *HST* spectrum to vary with time, we introduce a fit parameter which simply scales the strength of these absorption features. In particular, the normalized, scaled *HST* spectrum is calculated as $\text{flux}_{\text{HST,norm,scaled}} = 1 - (1 - \text{flux}_{\text{HST,norm}}) \times \text{scale fac}$

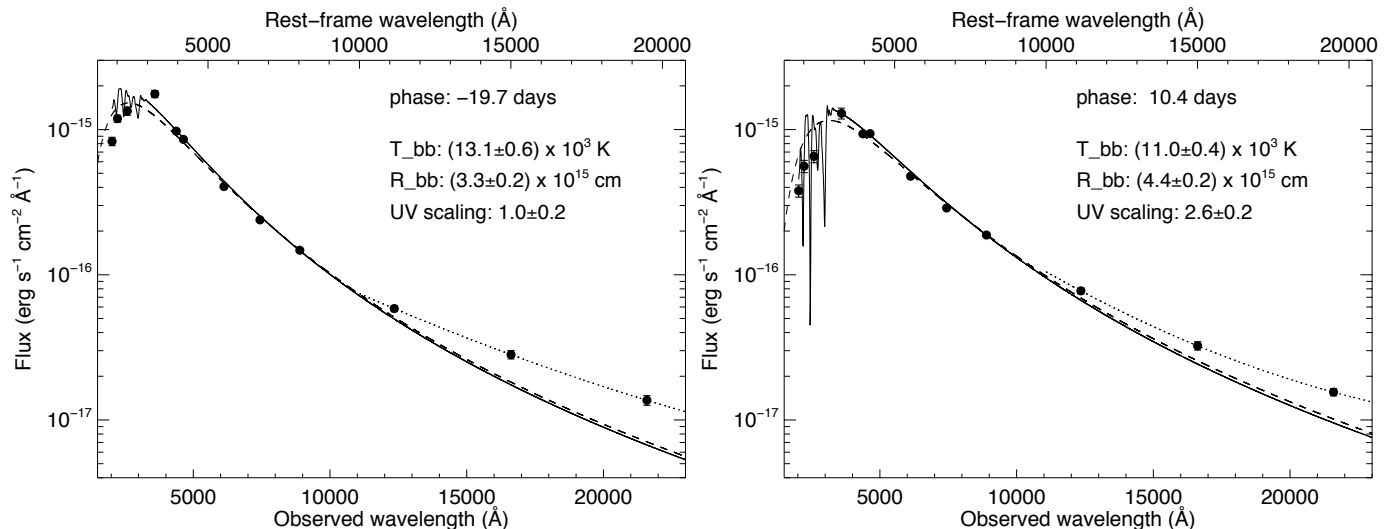


Figure 2. Two examples of Planck-function fits to the SEDs constructed from the photometry. The dashed lines show the best-fitting Planck function to the data, while the solid line depicts the best-fitting Planck function that has been modified below 3000 Å using an observed near-UV spectrum taken with *HST*. Simply comparing the near-UV magnitudes (the three data points on the left) with the *uBg* magnitudes suggests that the UV absorption is increasing with time. The dotted lines display a low-order polynomial fit to the NIR data, which is used to estimate the amount of NIR excess above the Planck fit. This NIR excess emission might be produced by re-emission of photons absorbed in the near-UV. The blackbody temperature, radius, and UV scaling factor derived from these fits are also listed (see the text for details).

tor. For example, in Fig. 2, the solid lines show the best-fitting modified blackbody spectrum. In the left panel, at a phase within a day of the epoch that the *HST* spectrum was taken, the UV absorption scaling was found to be around unity, as expected. On the right, the best-fit scale factor is much stronger, almost a factor of three. The third panel of Fig. 3 shows the best-fitting UV absorption scale factor for all epochs for which UV photometry is available; it is clearly increasing in time.

Interestingly, an increase in the UV absorption lines is also observed for iPTF 13ajg (Vreeswijk et al. 2014), one of the few SLSNe-I with good temporal coverage of the near-UV region where this can be measured. The increase is clear from Fig. 4 of Vreeswijk et al. (2014), where the spectra with UV coverage have been normalized by the blackbody fits. Measuring the combined equivalent width of the iPTF 13ajg model spectra in the rest-wavelength range of 2000–2800 Å for epochs 2–5, we obtain a linear increase in rest-frame equivalent width of 35% between phases –8 and +10 days. The corresponding increase in equivalent width (or increase in UV scale factor) for PTF 12dam over the same phase is very similar, 39%. However, the rest-frame equivalent width over the range 2000–2800 Å at phase –8 days is about a factor of three smaller for PTF 12dam compared to iPTF 13ajg: 200 Å for PTF 12dam versus 600 Å for iPTF 13ajg. An increase in the near-UV absorption is not unexpected: as the ejecta cool down from initially being very hot, the fraction of ions in the lower-ionization states increases, and these are thought to be responsible for the near-UV absorption lines (Mg II, C II, C III, Fe III).

The blackbody fits to the PTF 12dam photometry are consistently below the *JHK* flux measurements. The absorption in the UV could potentially be related to this excess emission in the NIR, as the absorbed UV emission is expected to be reradiated at longer wavelengths. This effect is observed in Type Ia SNe: the flux absorbed at blue wavelengths due to Fe II and Co II is redistributed to

the red, eventually leading to a NIR secondary maximum (e.g., see Figs. 4 and 5 of Pinto & Eastman 2000; Kasen & Woosley 2007).

We investigate if the NIR excess is related to the UV absorption in PTF 12dam by determining the absorbed UV flux over the rest-frame range 2000–3000 Å, and the excess NIR emission over the rest-frame range 1–2.5 μm. For the NIR excess determination, we approximate the observed spectrum with a low-order polynomial shown as dotted lines in Fig. 2, and integrate over the flux difference between this spectrum and the best-fitting blackbody (solid line). The inferred ratio of near-UV absorption over NIR excess shows a smooth evolution in time, starting at a factor of two at a phase of –20 days and reaching a factor of four at around –5 days, after which it very slowly decreases to a factor between 3.5 and 4 at +15 days. The wavelength upper limit of integration for the NIR excess of 2.5 μm is arbitrary; if we extend it to a longer wavelength the above factor of roughly four would decrease. We note that the NIR excess is apparent until a phase of +130 days, after which the blackbody fits are consistent with the optical through NIR flux measurements. The apparent additional NIR emission above the Planck fits could potentially be caused by photons being emitted at longer wavelengths following absorption in the UV part of the spectrum, but it is difficult to confirm this. The lack of NIR excess beyond +130 days can be explained by the SN temperature having decreased to around 5000 K at this point, resulting in very few available UV photons to be re-emitted in the NIR.

The resulting blackbody temperature, radius, UV absorption scale factor, and bolometric luminosity evolution are listed in Table 2 and shown in Fig. 3. The estimate of the bolometric luminosity includes a correction for the UV absorption as described by the straight-line fit to the scale factor shown in the third panel from the top. Adopting the temperature evolution estimated by the polynomial fit at early times, we also infer the black-

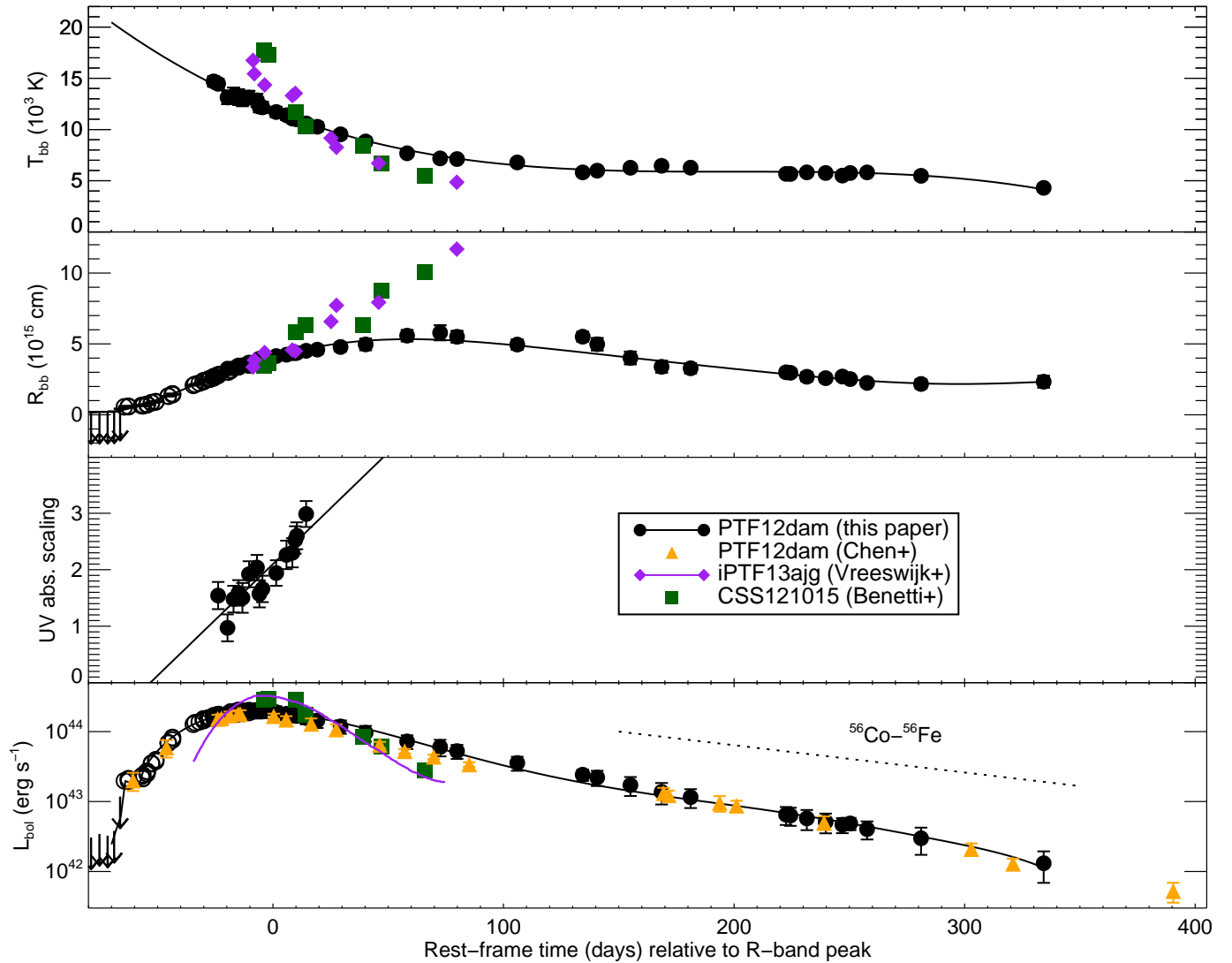


Figure 3. Time evolution of (from top to bottom) the blackbody effective temperature, blackbody radius, UV absorption strength scaling of observed *HST* spectrum, and bolometric luminosity of PTF 12dam compared to a few other SLSNe. The filled black circles correspond to the best-fit values inferred from the Planck-function fits to the SEDs constructed from the light curve, with fit parameters T_{bb} , R_{bb} , and UV absorption scale factor. The solid lines in the top three panels are polynomial fits to the best-fit values, and the solid black line in the lower panel is derived from these. The radii inferred from the early *r*-band data points alone (instead of the multifilter SEDs), adopting the temperature evolution shown in the top panel, are depicted by the open circles, as are the corresponding bolometric luminosity values. The filled circles in the bottom panel show the PTF 12dam bolometric light curve inferred from the T_{bb} and R_{bb} values and modified by the polynomial fit to the UV scaling. We also show the PTF 12dam bolometric light curve as inferred by Chen et al. (2015) and updated by Chen et al. (2016, Erratum, in prep.). The temperature, radius, and bolometric luminosity evolution of PTF 12dam are compared to a few other SLSNe: iPTF 13ajg (filled purple diamonds; Vreeswijk et al. 2014) and CSS 121015 (filled green squares; Benetti et al. 2014).

body radius from each *r*-band measurement before maximum light, which provides a rough estimate of the radius evolution at early times.

Integrating the bolometric light curve that we derive over the phase interval from -70 to $+334$ days results in an estimated total radiated energy of $E_{rad} = 1.8 \times 10^{51}$ erg for PTF 12dam. This value is similar to that found for other SLSNe, such as the Type I SNLS 06D4eu (Howell et al. 2013) and iPTF 13ajg (Vreeswijk et al. 2014) and the Type II CSS 121015 (Benetti et al. 2014).

3.2. iPTF 13dcc

Figure 4 shows the light curve of iPTF 13dcc. The *r*-band evolution displays an initial slow decline extending over at least 30 rest-frame days, after which the SLSN is rebrightening to reach its peak brightness around 60 rest-

frame days after the initial detection. The main peak brightness of the polynomial fit through the *r*-band data (shown by the solid line in Fig. 4) of $r = 19.5$ mag is reached at a modified Julian date of MJD = 56618.3, corresponding to UTC 2013 November 22.3. Although there is a gap in the data around the time of the peak, we adopt this date and magnitude as the main peak time and *r*-band magnitude of iPTF 13dcc. At this epoch, we determine a K-correction (see Hogg et al. 2002) from observed *r* to rest-frame SDSS *g* of -0.4 mag, leading to an absolute *g*-band peak magnitude of $M_{g, peak} = -22.0$ (the distance modulus of iPTF 13dcc is 41.93 mag). The absolute *g*-band magnitude is plotted on the right-hand axis of Fig. 4. At the redshift of iPTF 13dcc ($z = 0.431$), the effective wavelengths of observed *r* and rest-frame *g* match very well, leading to a

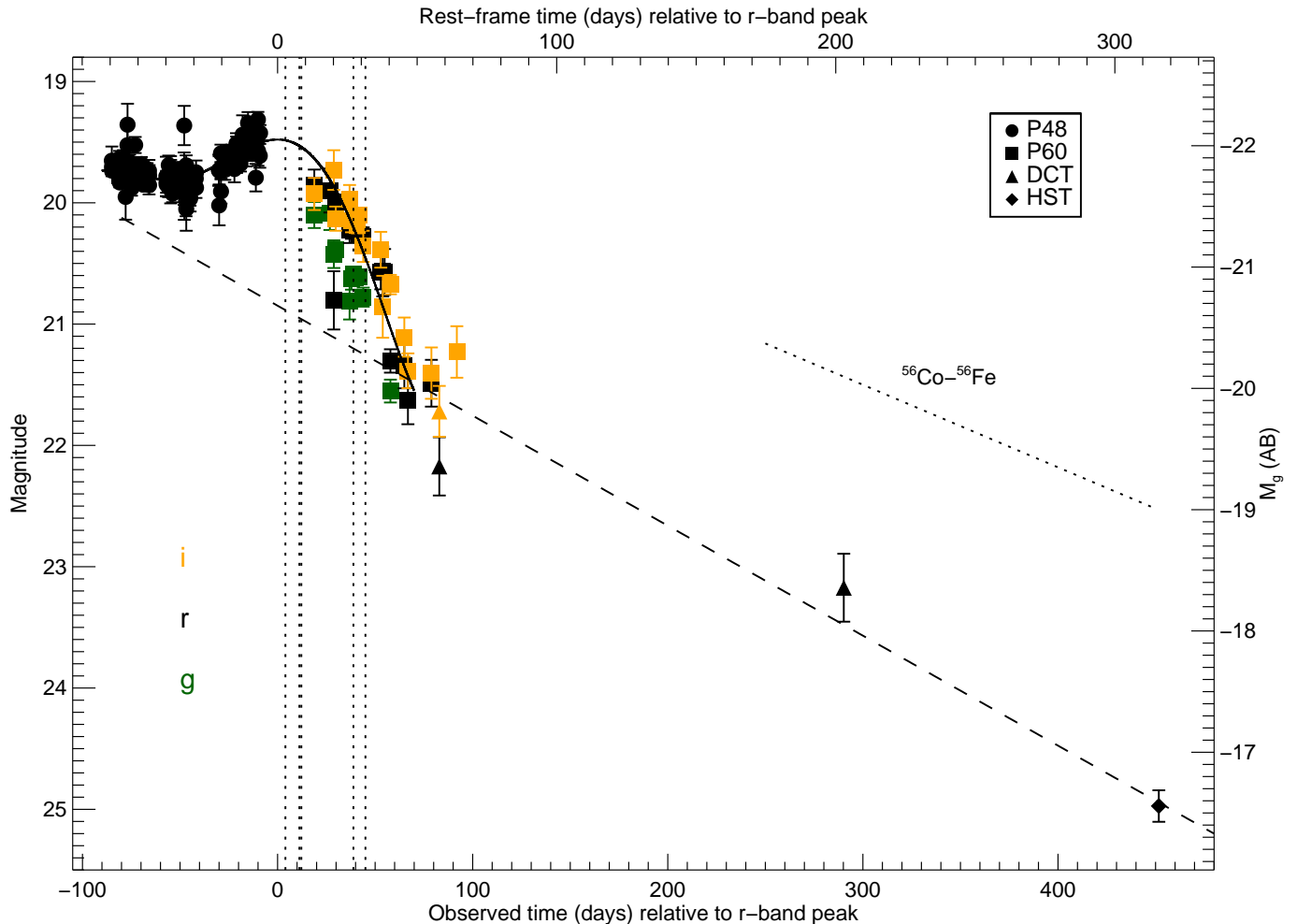


Figure 4. Light curves of iPTF 13dcc. Different colors and symbols denote different filters and telescopes, respectively. The solid line shows a polynomial fit to the r -band data up to about $t_{\text{obs}} = 70$ days. The dashed line displays a straight-line fit (i.e., exponential decay of the flux vs. linear time) to the last seven r -band data points. The late-time light curve is similar to the decay expected from radioactive decay of ^{56}Co to ^{56}Fe , as indicated by the slanted dotted line. The vertical dotted lines show the epochs at which the iPTF 13dcc spectra were obtained.

K-correction that is almost independent of the color evolution of the SN with a magnitude depending mainly on the redshift: $K_{rg} = -2.5 \log(1+z) = -0.4$.

The apparent r -band brightness of the early excess emission is only a few tenths of a magnitude fainter than the brightness at peak, and the early decline suggests it probably was even brighter before. iPTF or other surveys did not observe this sky location during several months prior to our first detection, so we do not have any constraints on the early brightness evolution and the time of explosion. After the main peak, the light curve is declining rapidly until about 50 days after peak, followed by a very slow late-time decay with a slope that is only slightly steeper than that expected from the decay of radioactive ^{56}Co , assuming full trapping of the gamma-ray photons produced.

Since we do not have any information on the iPTF 13dcc light-curve evolution before our first detection, it is possible that the main peak occurred earlier and that the peak we consider to be the main peak is a late-time rebrightening. Such a rebrightening has been detected in other SLSNe, such as SN2015bn (Nicholl et al. 2016). However, in the case of iPTF 13dcc, the current main peak reaches an absolute g -band magnitude of

$M_g = -22.0$. If this is a late-time rebrightening similar to that of SN2015bn, the main peak would have reached around $M_g \approx -23$, which would be stretching the brightness budget of SLSNe. Also, below we show that the estimated temperature of iPTF 13dcc at the presumed peak is very similar to that of various other SLSNe-I at peak. If indeed the actual main peak occurred before our first detection, we would have expected the temperature at the time of this supposed rebrightening to be well below 10,000 K. For these reasons, we consider it unlikely that the actual main peak occurred before our first detection.

The light curve of iPTF 13dcc is rather limited in multifilter observations, making it difficult to derive a bolometric light curve from the photometry as we did for PTF 12dam. Instead, we turn to the spectroscopic sequence that was secured for this source as part of the iPTF follow-up campaign; see Table 1 and Fig. 5. The times at which the five iPTF 13dcc spectra were taken, ranging from around the main peak until +30 days in the rest frame, are indicated by the vertical dotted lines in Fig. 4. For each spectrum, we fit a Planck function to selected wavelength regions of the continuum free from obvious features (these regions are indicated with the short dashes at the top of the figure). This results in a

Table 2
Blackbody temperature, radius, and bolometric luminosity of PTF 12dam.

Phase (days)	T_{bb} (10^3 K)	R_{bb} (10^{15} cm)	$\log L_{\text{bol}}$ (erg s^{-1})
-78.86		< 0.19	< 42.49
-75.24		< 0.21	< 42.54
-71.68		< 0.21	< 42.51
-68.86		< 0.23	< 42.58
-66.28		< 0.42	< 43.07
-25.71	14.69 \pm 0.52	2.57 \pm 0.11	44.21 \pm 0.07
-23.76	14.46 \pm 0.47	2.71 \pm 0.11	44.24 \pm 0.06
-19.69	13.13 \pm 0.64	3.26 \pm 0.20	44.25 \pm 0.09
-17.06	13.32 \pm 0.77	3.28 \pm 0.24	44.28 \pm 0.10
-14.89	13.17 \pm 0.77	3.39 \pm 0.25	44.29 \pm 0.11
-13.22	12.99 \pm 0.71	3.49 \pm 0.24	44.29 \pm 0.10
-10.37	13.11 \pm 0.66	3.50 \pm 0.23	44.31 \pm 0.09
-6.92	12.85 \pm 0.65	3.64 \pm 0.24	44.31 \pm 0.09
-5.87	12.23 \pm 0.56	3.91 \pm 0.24	44.30 \pm 0.09
-4.54	12.16 \pm 0.55	3.94 \pm 0.24	44.30 \pm 0.08
1.44	11.71 \pm 0.51	4.14 \pm 0.24	44.28 \pm 0.08
5.89	11.39 \pm 0.45	4.24 \pm 0.24	44.25 \pm 0.08
8.45	11.07 \pm 0.43	4.35 \pm 0.23	44.23 \pm 0.08
9.69	11.04 \pm 0.43	4.35 \pm 0.24	44.23 \pm 0.08
10.39	10.99 \pm 0.43	4.37 \pm 0.24	44.22 \pm 0.08
14.42	10.59 \pm 0.40	4.52 \pm 0.24	44.19 \pm 0.07
19.26	10.27 \pm 0.45	4.60 \pm 0.30	44.16 \pm 0.09
29.34	9.53 \pm 0.41	4.78 \pm 0.31	44.07 \pm 0.08
40.21	8.83 \pm 0.42	4.97 \pm 0.40	43.98 \pm 0.10
58.20	7.68 \pm 0.33	5.58 \pm 0.40	43.86 \pm 0.09
72.52	7.18 \pm 0.35	5.79 \pm 0.53	43.78 \pm 0.10
79.85	7.12 \pm 0.30	5.50 \pm 0.41	43.72 \pm 0.09
105.98	6.79 \pm 0.29	4.95 \pm 0.37	43.55 \pm 0.09
134.35	5.81 \pm 0.20	5.51 \pm 0.34	43.38 \pm 0.07
140.65	5.98 \pm 0.26	4.98 \pm 0.44	43.34 \pm 0.10
155.05	6.27 \pm 0.32	4.01 \pm 0.45	43.24 \pm 0.11
168.56	6.46 \pm 0.37	3.39 \pm 0.43	43.14 \pm 0.13
181.16	6.27 \pm 0.32	3.28 \pm 0.36	43.06 \pm 0.11
222.56	5.67 \pm 0.28	3.00 \pm 0.31	42.81 \pm 0.11
224.44	5.66 \pm 0.28	2.96 \pm 0.31	42.80 \pm 0.11
231.57	5.81 \pm 0.31	2.68 \pm 0.32	42.76 \pm 0.12
239.73	5.75 \pm 0.30	2.58 \pm 0.30	42.71 \pm 0.12
246.99	5.50 \pm 0.24	2.70 \pm 0.23	42.67 \pm 0.09
250.37	5.75 \pm 0.19	2.52 \pm 0.19	42.69 \pm 0.08
257.69	5.81 \pm 0.29	2.25 \pm 0.24	42.61 \pm 0.11
281.11	5.48 \pm 0.41	2.17 \pm 0.32	42.47 \pm 0.15
334.29	4.30 \pm 0.35	2.33 \pm 0.41	42.12 \pm 0.17

best-fit blackbody temperature, radius, and corresponding bolometric luminosity at each epoch, shown by the filled black circles in the top, middle, and bottom panels of Fig. 6, respectively. These values correspond to the bold-faced entries in Table 3. The iPTF 13dcc spectra and the blackbody fits are shown in Fig. 5.

The temporal range spanned by the spectra is limited, from the time of the main peak to +30 rest-frame days. Therefore, to estimate the full bolometric light curve we have to make an assumption about the iPTF 13dcc temperature evolution outside of this range. In the top panel of Fig. 6, we also show the inferred temperature evolution of PTF 12dam (derived in Sec. 3.1), CSS 121015 (Benetti et al. 2014), iPTF 13ajg (Vreeswijk et al. 2014), and DES 14X3taz (Smith et al. 2016). The temperature derived from the iPTF 13dcc spectra appears to match the evolution of PTF 12dam quite well. However, it is also not too far from the temperature evolution of the other SLSNe-I that are shown.

Assuming a particular temperature evolution and that iPTF 13dcc is radiating as a blackbody, our r -band photometry can be used to infer the radius evolution. This is done assuming the temperature evolu-

Table 3
Blackbody temperature (adopted from PTF 12dam), radius, and bolometric luminosity of iPTF 13dcc.

Phase (days)	T_{bb} (10^3 K)	R_{bb} (10^{15} cm)	$\log L_{\text{bol}}$ ($[\text{erg s}^{-1}]$)
-59.33	18.80	2.50 \pm 0.04	44.75 \pm 0.07
-56.54	18.39	2.52 \pm 0.03	44.71 \pm 0.06
-55.82	18.29	2.51 \pm 0.05	44.70 \pm 0.08
-55.17	18.19	2.58 \pm 0.05	44.71 \pm 0.08
-54.43	18.08	2.34 \pm 0.20	44.62 \pm 0.15
-53.79	17.99	2.71 \pm 0.09	44.74 \pm 0.10
-53.03	17.89	2.67 \pm 0.05	44.72 \pm 0.08
-52.32	17.79	2.56 \pm 0.04	44.67 \pm 0.07
-51.01	17.60	2.94 \pm 0.09	44.77 \pm 0.10
-50.24	17.49	2.58 \pm 0.04	44.65 \pm 0.07
-49.54	17.40	2.66 \pm 0.06	44.66 \pm 0.08
-48.83	17.30	2.72 \pm 0.04	44.67 \pm 0.07
-48.13	17.20	2.67 \pm 0.03	44.65 \pm 0.06
-47.40	17.10	2.69 \pm 0.03	44.64 \pm 0.06
-46.71	17.01	2.68 \pm 0.04	44.63 \pm 0.07
-46.04	16.92	2.70 \pm 0.06	44.63 \pm 0.09
-39.80	16.10	2.82 \pm 0.08	44.58 \pm 0.10
-39.02	16.00	2.89 \pm 0.06	44.59 \pm 0.08
-38.32	15.92	2.95 \pm 0.07	44.60 \pm 0.09
-37.63	15.83	2.84 \pm 0.06	44.56 \pm 0.08
-36.94	15.74	2.91 \pm 0.05	44.57 \pm 0.08
-36.25	15.66	2.97 \pm 0.05	44.58 \pm 0.07
-35.56	15.57	3.01 \pm 0.04	44.58 \pm 0.07
-34.86	15.49	2.93 \pm 0.05	44.55 \pm 0.08
-34.15	15.40	3.05 \pm 0.05	44.57 \pm 0.08
-33.45	15.31	3.17 \pm 0.17	44.60 \pm 0.12
-32.75	15.23	2.99 \pm 0.09	44.54 \pm 0.10
-32.06	15.15	3.04 \pm 0.08	44.54 \pm 0.09
-31.37	15.06	2.95 \pm 0.06	44.50 \pm 0.08
-29.26	14.82	3.13 \pm 0.06	44.53 \pm 0.08
-20.96	13.88	3.39 \pm 0.12	44.48 \pm 0.10
-20.26	13.81	3.55 \pm 0.07	44.51 \pm 0.08
-19.53	13.73	3.62 \pm 0.09	44.52 \pm 0.09
-18.85	13.66	3.74 \pm 0.05	44.54 \pm 0.07
-18.13	13.58	3.80 \pm 0.04	44.54 \pm 0.06
-15.39	13.29	3.86 \pm 0.09	44.52 \pm 0.08
-14.68	13.22	4.03 \pm 0.09	44.55 \pm 0.08
-13.98	13.15	4.00 \pm 0.08	44.53 \pm 0.08
-13.30	13.08	4.03 \pm 0.07	44.53 \pm 0.07
-12.59	13.01	4.19 \pm 0.07	44.55 \pm 0.08
-11.24	12.88	4.28 \pm 0.15	44.56 \pm 0.10
-10.52	12.80	4.49 \pm 0.08	44.59 \pm 0.08
-9.74	12.73	4.28 \pm 0.05	44.53 \pm 0.06
-9.03	12.66	4.35 \pm 0.07	44.54 \pm 0.07
-7.71	12.53	4.39 \pm 0.09	44.53 \pm 0.08
-7.02	12.47	4.73 \pm 0.11	44.59 \pm 0.08
-6.30	12.40	4.57 \pm 0.12	44.55 \pm 0.09
2.81	11.65 \pm 2.46	5.28 \pm 0.44	44.56 \pm 0.27
7.81	10.91 \pm 0.40	5.44 \pm 0.20	44.48 \pm 0.07
8.50	10.66 \pm 0.34	5.55 \pm 0.19	44.45 \pm 0.06
13.16	10.73	4.79 \pm 0.29	44.33 \pm 0.13
18.75	10.31	5.00 \pm 0.42	44.30 \pm 0.15
20.16	10.20	3.35 \pm 0.37	43.94 \pm 0.17
20.84	10.15	4.90 \pm 0.10	44.26 \pm 0.08
25.80	9.81	4.67 \pm 0.23	44.16 \pm 0.12
26.47	9.77	4.71 \pm 0.16	44.16 \pm 0.10
27.15	9.72	4.83 \pm 0.07	44.17 \pm 0.07
27.17	7.42 \pm 0.76	7.29 \pm 0.51	44.06 \pm 0.16
27.84	9.67	4.78 \pm 0.09	44.15 \pm 0.08
29.26	9.58	4.77 \pm 0.11	44.13 \pm 0.08
30.70	9.49	4.82 \pm 0.17	44.13 \pm 0.10
31.48	8.45 \pm 0.74	5.56 \pm 0.34	44.05 \pm 0.14
36.98	9.10	4.53 \pm 0.30	44.00 \pm 0.13
37.68	9.06	4.58 \pm 0.43	44.00 \pm 0.16
38.37	9.02	4.60 \pm 0.40	44.00 \pm 0.15
40.43	8.90	3.36 \pm 0.15	43.70 \pm 0.11
45.41	8.63	3.50 \pm 0.30	43.69 \pm 0.15
46.72	8.56	3.12 \pm 0.28	43.57 \pm 0.15
55.12	8.15	3.66 \pm 0.33	43.62 \pm 0.15
57.95	8.02	2.76 \pm 0.31	43.35 \pm 0.17
202.87	5.88	3.58 \pm 0.46	43.04 \pm 0.18
315.76	4.78	2.90 \pm 0.17	42.49 \pm 0.13

Note. — The bold-faced values are inferred from the iPTF 13dcc spectra, while for the others the PTF 12dam temperature evolution was adopted with the radii inferred using the r -band magnitude.

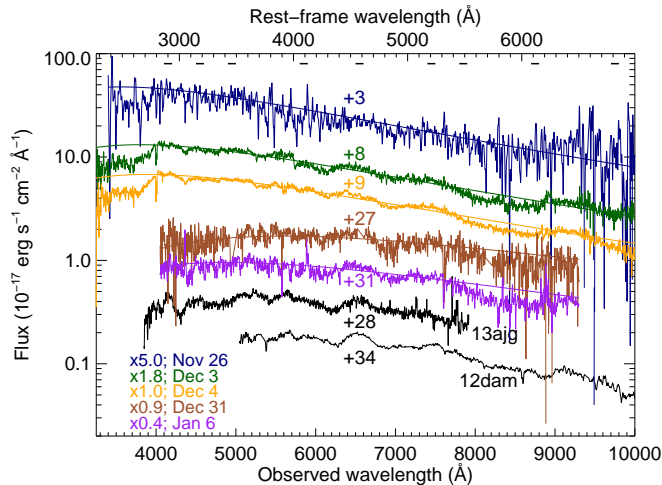


Figure 5. Time series of spectra of iPTF 13dcc (see Table 1). The spectra were corrected for Galactic extinction (Schlafly & Finkbeiner 2011) and scaled to the polynomial fit to the r -band photometry depicted in Fig. 4 to ensure a proper absolute calibration. To avoid the spectra overlapping each other, an additional scaling was applied as indicated at the bottom left, along with the date of observation (Nov./Dec. 2013 and Jan. 2014); the phase (rest-frame days relative to the r -band maximum) is shown next to each spectrum. The iPTF 13dcc spectra were smoothed with a Gaussian filter having a full width at half-maximum intensity (FWHM) of 5 Å. The spectra were fit with a Planck function to selected 50 Å-wide wavelength regions (the same for all spectra; these regions are indicated with dashes at the top of the plot). For comparison, we show the spectra of two known SLSNe-I at the bottom in black: iPTF 13ajg (Vreeswijk et al. 2014) and PTF 12dam (Nicholl et al. 2013) at phases of +28 and +34 days, respectively.

tion of different SLSNe: PTF 12dam, iPTF 13ajg, and DES 14X3taz. The resulting radius evolution for each of these three cases is shown by the solid lines in the middle panel of Fig. 6. The radius evolution adopting the DES 14X3taz temperature appears contrived; if the temperature evolved that dramatically for iPTF 13dcc as well, we would have detected it in our r -band photometry. In principle, it is possible that the iPTF 13dcc temperature evolution contained a similar dramatic drop and rise as DES 14X3taz, but if it did that must have occurred before our first r -band detection. The middle panel also shows the radii inferred directly from the iPTF 13dcc spectra (filled black circles), the radius evolution inferred for PTF 12dam (dashed black line, see Sec. 3.1), and that inferred for DES 14X3taz by Smith et al. (2016).

The bottom panel of Fig. 6 shows the bolometric luminosity evolution of iPTF 13dcc adopting the temperature evolution of PTF 12dam, iPTF 13ajg, and DES 14X3taz. As mentioned above, the latter appears contrived and we consider it irrelevant for iPTF 13dcc, whereas adopting the temperature evolution of iPTF 13ajg leads to unreasonably large values for the early-time bolometric luminosity of iPTF 13dcc. We therefore adopt the temperature evolution of PTF 12dam to derive the bolometric light curve of iPTF 13dcc, listed in Table 3 and shown by the open circles in the bottom panel of Fig. 6. We will adopt this bolometric evolution of iPTF 13dcc when performing the modelling in Sec. 4. Integrating this bolometric light curve over the phase interval from -59 to $+60$ days (-59 to $+315$ days) results in an estimated total radiated energy of $E_{\text{rad}} = 2.8 \times 10^{51}$ erg

(3.0×10^{51} erg) for iPTF 13dcc, which is about 60% larger than the value we derived for PTF 12dam (see Sec. 3.1). For comparison, we also show the bolometric evolution of PTF 12dam, CSS 121015, iPTF 13ajg, and DES 14X3taz.

Finally, we also plot the pair-instability supernova (PISN) model denoted R190 from Dessart et al. (2012), scaled up in luminosity ($\times 15$) and shifted and contracted in time ($\times 0.45$) to best match the bolometric behavior of iPTF 13dcc. The time of the main peak (i.e., at phase = 0 in the figure) of the unscaled R190 model is about 220 days after explosion, or 100 days in the contracted model shown. Dessart et al. (2012) focus on three types of PISN, with the stars exploding being a red supergiant (RSG), a blue supergiant (BSG), or a Wolf-Rayet (WR) star (see also Dessart et al. 2013). The R190 model refers to a $190 M_{\odot}$ main-sequence star dying as a $164 M_{\odot}$ RSG with a surface radius of about $4000 R_{\odot}$ and an extended hydrogen envelope. Despite the R190 model being scaled both in luminosity and time, the similarity in the general brightness evolution with iPTF 13dcc is intriguing. However, this model with a hydrogen envelope is not the most natural for explaining the observations of a hydrogen-poor SLSN. In addition, Jerkstrand et al. (2016) compare their PISN models with the nebular spectra of SN 2007bi and PTF 12dam, finding discrepancies for several key observables and thus no support for a PISN interpretation.

4. MODELLING

In this section, we explore different light-curve models that could explain the bolometric light-curve evolution of PTF 12dam and iPTF 13dcc derived in the previous section. We start by applying the semi-analytical light-curve models described by Chatzopoulos et al. (2012) and Chatzopoulos et al. (2013). These include the following three independent power inputs: (1) radioactive decay of ^{56}Ni and ^{56}Co , (2) magnetar spin-down, and (3) forward- and reverse-shock heating due to SN ejecta interacting with CSM. The radioactive decay and interaction power inputs have also been combined by Chatzopoulos et al. (2012) into a hybrid model in which both processes can be modelled simultaneously. These models are described in more detail below, but we also refer the reader to the above-mentioned papers.

In addition, we investigate if the early-time bump or plateau observed in PTF 12dam and iPTF 13dcc could be produced by cooling emission from material heated by the shock produced in the explosion. For standard SNe, the expected cooling emission has been modelled with the material being the outer part of the stellar envelope (Rabinak & Waxman 2011) and also for the case in which an extended low-mass envelope is surrounding a compact core (Nakar & Piro 2014).

Nakar & Piro (2014) show that a standard progenitor cannot explain the fast drop in bolometric luminosity after the first peak, which is supported by comparison of the Rabinak & Waxman (2011) model to observations of SLSNe with double-peaked light curves: LSQ 14bdq (Nicholl et al. 2015) and DES 14X3taz (Smith et al. 2016). Although Sapir & Waxman (2016) extend the Rabinak & Waxman analytic expressions to later times and do infer a drop in luminosity for normal SNe-II, their model is strictly valid only at times when the photospheric (i.e. effective) temperature is above the recombination temperature for the opacity in the relevant outer

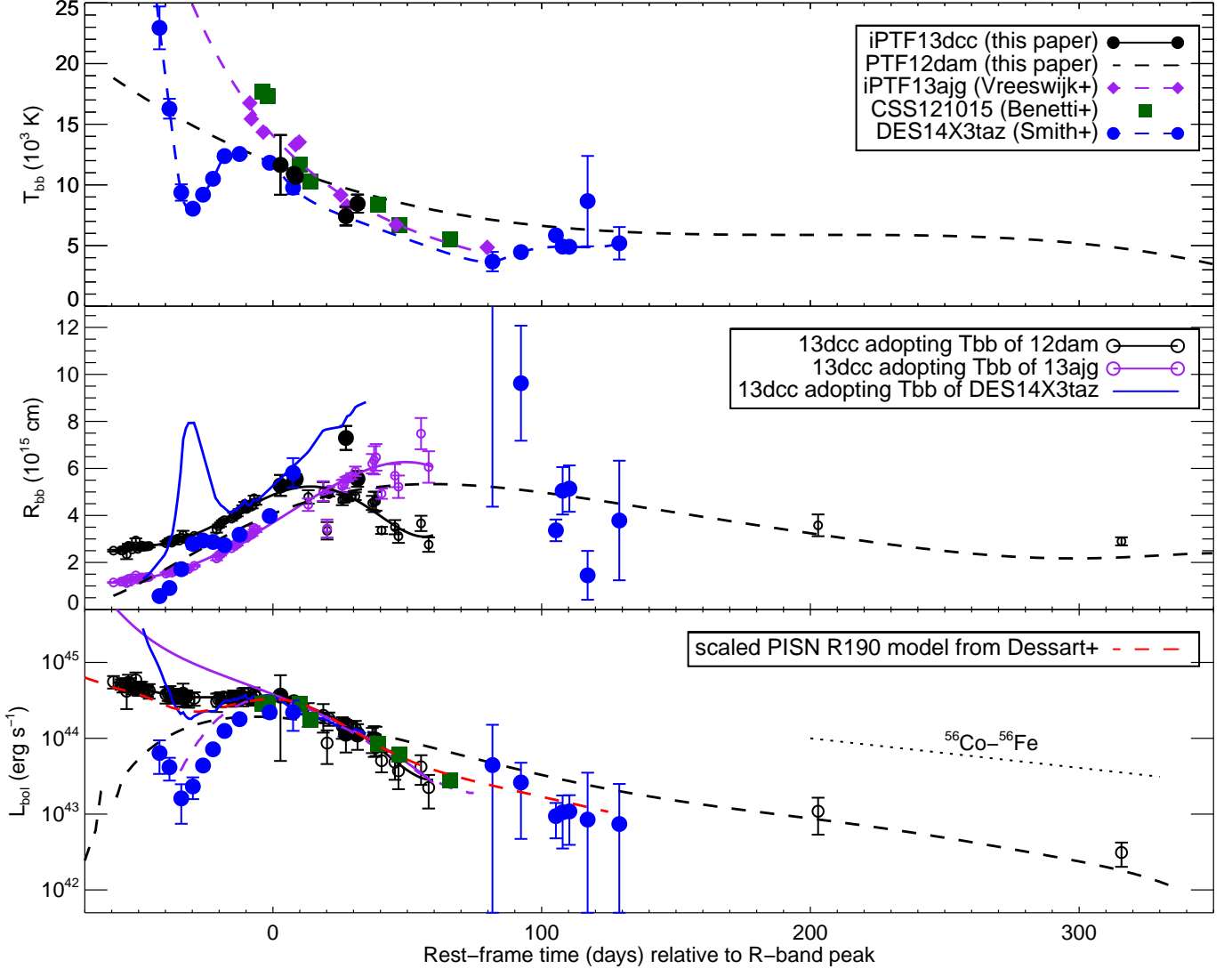


Figure 6. Time evolution of (from top to bottom) the blackbody temperature, radius, and bolometric luminosity of iPTF 13dcc. The filled black circles in all panels correspond to the best-fit values inferred from the Planck-function fits to the spectra, with fit parameters T_{bb} and R_{bb} . **Top panel:** the temperature evolution of iPTF 13dcc is compared to that inferred for PTF 12dam (open black triangles and dashed line), CSS 121015 (green squares; Benetti et al. 2014), iPTF 13ajg (purple diamonds; Vreeswijk et al. 2014), and DES 14X3taz (filled blue circles; Smith et al. 2016). **Middle panel:** the radius evolution of iPTF 13dcc inferred from our r -band observations, adopting the temperature evolution of PTF 12dam (small open black circles and solid line), iPTF 13ajg (small open purple circles and solid line), and DES 14X3taz (solid blue line). The filled blue circles show the radius evolution inferred for DES 14X3taz by Smith et al. (2016). The black dashed line shows the radius evolution that we inferred for PTF 12dam (see Fig. 3). **Bottom panel:** the iPTF 13dcc bolometric light curve inferred from the polynomial fits to the radius and assuming the temperature evolution of PTF 12dam (open black circles), iPTF 13ajg (solid purple line), and DES 14X3taz (solid blue line). These are compared with the evolution inferred for PTF 12dam (dashed black line), CSS 121015 (filled green squares), iPTF 13ajg (dashed purple line), DES 14X3taz (filled blue circles), and the pair-instability supernova (PISN) R190 model from Dessart et al. (2012), scaled and shifted to match the peak of iPTF 13dcc (red dashed line).

shells of the envelope to be time and space independent. For hydrogen-poor envelopes this latter temperature is of the order of the recombination temperature of doubly-ionized helium: 2–2.5 eV or 23–29 kK, and so this model is not applicable to PTF 12dam or iPTF 13dcc where the early excess emission peak occurs at around 10 days when the effective temperature has already dropped well below this temperature limit. For both LSQ 14bdq and DES 14X3taz, shock cooling of an extended envelope appears to describe the initial peak rather well (Piro 2015; Smith et al. 2016). We therefore focus on the extended envelope case, following the prescription of Piro (2015). We note that this model also successfully reproduces the early bump of iPTF 15dtg, a spectroscopically normal

SN Ic from a massive progenitor (Taddia et al. 2016).

Finally, we combine the Piro model with the Chatzopoulos magnetar and CSM interaction models to fit the entire bolometric light curve of iPTF 13dcc. In the CSM case, this has the advantage that two fit parameters are the same in these models: the total SN energy, and the sum of Piro’s core and extended mass is the same as the ejecta mass in the CSM interaction model. For PTF 12dam the early excess emission has too few data points to attempt this combined modelling. As a comparison for the best-fit values inferred for PTF 12dam and iPTF 13dcc, we also fit all the above-mentioned models, including the combined ones, to the bolometric light curve of DES 14X3taz presented by Smith et al. (2016).

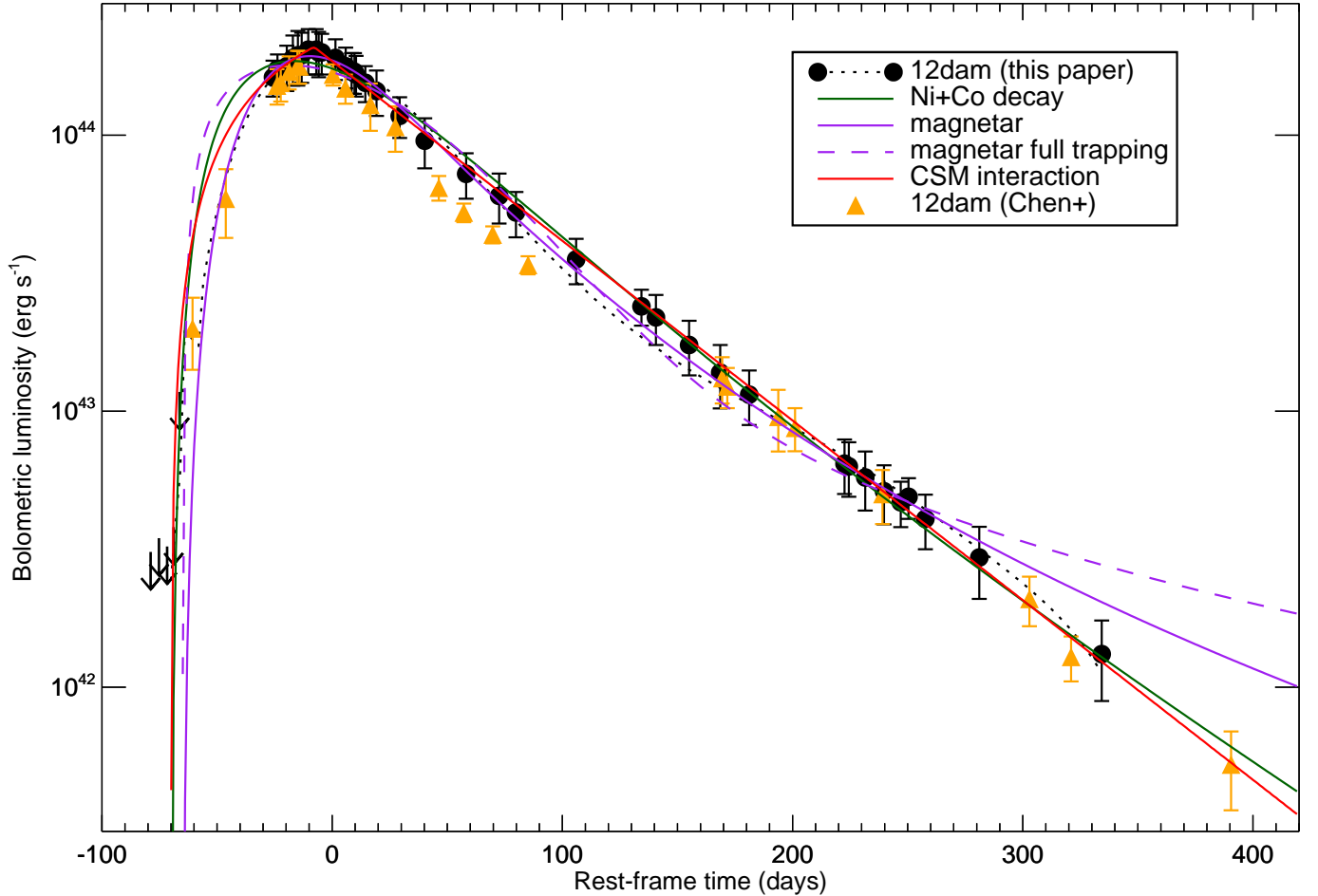


Figure 7. Model fits of radioactive decay (solid green line), magnetar (solid and dashed purple lines), and CSM interaction (solid red line) to the bolometric light curve of PTF 12dam that we derived in Sec. 3 (filled black circles and dotted line). See Tables 4, 5, and 6 for the corresponding parameter best-fit values. All three models provide a good description of the PTF 12dam data. The magnetar fits including increased leakage of energy as a function of time and assuming full trapping are shown with the solid and dashed purple lines, respectively. The filled orange triangles show the PTF 12dam bolometric light curve as inferred by Chen et al. (2015) and updated by Chen et al. (2016, Erratum, in prep.).

4.1. PTF 12dam

Figure 7 features the bolometric light curve of PTF 12dam as derived in Sec. 3. Around peak, the bolometric luminosity that we find is up to 50% higher than the PTF 12dam bolometric luminosity evolution derived by Nicholl et al. (2013) and Chen et al. (2015). In private communication with the first authors of these papers to try to understand this discrepancy, it was found that they used the wrong photometric zeropoints to convert the *Swift* UV magnitudes to fluxes (the zeropoint for Vega was used while the magnitudes published by Nicholl et al. and Chen et al. are in the AB system), leading to an underestimate of the true bolometric luminosity (see the Errata of Chen et al. 2016, in prep. and Nicholl et al. 2013²⁶). Correcting the Chen et al. bolometric light curve for this calibration error brings it up to a similar luminosity level as our bolometric light curve. In Fig. 7 we show the *corrected* bolometric light curve from the Erratum of Chen et al. 2016 (in prep.), which is still slightly below our light curve around peak and up to a phase of 100 days.

We fit the Chatzopoulos models to our light-curve data (the filled circles shown in Fig. 7) using a custom IDL χ^2 minimization program, in which we make grateful use of the MPFIT procedures²⁷ written by Craig Markwardt (Markwardt 2009; Moré 1978). Where relevant, we adopt a Thomson electron scattering opacity of $\kappa = 0.2 \text{ cm}^2 \text{ g}^{-1}$, appropriate for material without hydrogen, and also fit for the time of explosion which is assumed to be within the phase range of -70 to -65 days as constrained by the observations. We loosely limit the progenitor radius, R_0 , to be within the range $0.1\text{--}500 R_\odot$, and use a fiducial value for the expansion velocity of $v_{\text{exp}} = 10,000 \text{ km s}^{-1}$ for the radioactive decay and magnetar models (for the CSM interaction case this velocity is not assumed but is calculated in the model).

The power input in the first model that we fit is radioactive decay of ^{56}Ni and ^{56}Co , which produces energetic gamma rays that are thermalized in the expanding ejecta. The fit parameters are the time of explosion ($t_{\text{expl,rest}}$), the nickel mass produced (M_{Ni}), the mean of the hydrodynamical and diffusion timescales or effective light-curve timescale (t_d), a factor determining

²⁶ published online at <http://www.nature.com/nature/journal/v539/n7630/full/nature19850.html>

²⁷ see <http://purl.com/net/mpfit>

Table 4
Ni+Co decay best-fit parameters.

	PTF 12dam	iPTF 13dcc	DES 14X3taz ^a
$t_{\text{expl,rest}}$ [d]	-70 ^b	-89	-43 ^b
M_{Ni} [M_{\odot}]	21.9 ± 0.5	115 ± 209	26 ± 39
t_d [d]	46 ± 2	64 ± 25	61 ± 48
A_{leakage} [10^3 d^2]	28 ± 1	3 ± 8	4 ± 7
R_0 [R_{\odot}]	0.1 ^b	0.1 ^b	0.1 ^b
χ^2/DOF	5.9/32	119/51	73/10

^a For DES 14X3taz the first two detections have been discarded in the fit, focussing on fitting the main peak.

^b Parameter reached limit of allowed range.

the fraction of gamma rays that escape as a function of time (A_{leakage} , modifying the luminosity with the factor $1 - e^{-At^{-2}}$; i.e., a large A corresponds to full trapping), and the progenitor radius (R_0). The goodness-of-fit χ^2 value divided by the number of degrees of freedom (DOF) and best-fit values for the Ni+Co decay-model parameters are listed in Table 4, and the corresponding best fit to the PTF 12dam luminosity evolution is shown by the solid green line in Fig. 7.

This model describes the data very well. The very low reduced χ^2 indicates that the uncertainties in the luminosity are likely overestimated. However, the best-fit nickel mass, $M_{\text{Ni}} = 22 M_{\odot}$, is much greater than the estimated ejecta mass, $M_{\text{ej}} \approx 8 M_{\odot}$, which is calculated using Eq. 1 of Wheeler et al. (2015), repeated here:

$$M_{\text{ej}} \approx \frac{1}{2} \frac{\beta c}{\kappa} v_{\text{exp}} t_d^2, \quad (1)$$

where we have substituted the rise time to maximum light (t_r) with t_d , β is a constant of integration (13.8), and c is the speed of light. We note that this estimate of the ejecta mass is uncertain due to various assumptions made in its derivation, amongst others regarding the effective opacity and homologous expansion. Nonetheless, this model can probably be rejected on the basis that the required nickel mass to power the peak luminosity of PTF 12dam is unrealistically large (see also Nicholl et al. 2013; Chen et al. 2015). We note that Nicholl et al. (2013) inferred a lower nickel mass of 14–16 M_{\odot} (see their extended data Fig. 6) than we do, because they underestimated the true bolometric luminosity around peak of PTF 12dam, as we discussed above.

To check if the light curve tail can be powered by radioactive decay, we fit our late-time data beyond 100 rest-frame days. The nickel mass required (12 M_{\odot}) is still large for the estimated ejecta mass (22 M_{\odot} , which is larger than before because the best-fit effective diffusion time scale increased for this late-time fit). For the light curve beyond 200 days, the best nickel mass (10 M_{\odot}) and estimated ejecta mass (140 M_{\odot}) are compatible. Therefore, the radioactive decay of ^{56}Ni and ^{56}Co has difficulty accounting for the full bolometric light curve of PTF 12dam, but it could be that it is powering the late-time light curve.

In the magnetar model, the energy input is produced by the spin-down of a rapidly spinning, highly magnetic neutron star, the remnant of the explosion. Although it is not yet clear if and how a large fraction of the rotational and/or magnetic energy can be converted to radia-

Table 5
Magnetar best-fit parameters.

	PTF 12dam	iPTF 13dcc	DES 14X3taz ^a
$t_{\text{expl,rest}}$ [d]	-65 ^b	-70 ^b	-43 ^b
$P_{\text{sp,init}}$ [ms]	2.30 ± 0.03	1.69 ± 0.38	1.8 ± 2.8
B_{14} [10^{14} G]	0.7 ± 0.7	0.33 ± 0.18	0.39 ± 0.68
t_d [d]	50 ± 27	10 ^b	49 ± 202
A_{leakage} [10^3 d^2]	32 ± 51	7 ± 4	3 ± 11
R_0 [R_{\odot}]	0.1 ^b	0.1 ^b	0.1 ^b
χ^2/DOF	5.9/31	127/50	33.7/9

^a For DES 14X3taz the first two detections have been discarded in the fit, focussing on fitting the main peak.

^b Parameter reached limit of allowed range.

tion, in this model it is assumed that the energy from the magnetar is thermalized in the expanding ejecta. The parameters of the magnetar model are the time of explosion ($t_{\text{expl,rest}}$), the initial spin period of the neutron star in milliseconds ($P_{\text{sp,init}}$), its magnetic field strength in units of 10^{14} Gauss (B_{14}), the effective light-curve timescale (t_d), a constant A_{leakage} , and the progenitor radius (R_0). The parameters' best-fit values are listed in Table 5, and the corresponding best-fit model to the bolometric light curve of PTF 12dam is shown by the solid purple line in Fig. 7.

Although it is not present in Eq. 2 of Chatzopoulos et al. (2013), we include a leakage factor in exactly the same way as is done for the radioactive decay model (see also Wang et al. 2015). We stress that when assuming full trapping (i.e., a large value for A_{leakage}), the magnetar model predicts a late-time luminosity brighter than the observations, as already found by Chen et al. (2015). We show this full-trapping model fit with the dashed purple line in Fig. 7, which has best-fit values $P_{\text{sp,init}} = 1$ ms (reaching the lower limit of the allowed range) and $B_{14} = 1.63 \pm 0.03$ G ($\chi^2/\text{DOF} = \chi_{\nu}^2 = 0.7$). The magnetar model including the leakage factor fits our data well ($\chi_{\nu}^2 = 0.2$). In the radioactive decay model, the leakage is understood: the opacity of the gamma rays produced in the radioactive decay of nickel and cobalt is decreasing with time, allowing an increasing fraction of the energy to escape. In the magnetar model, however, it is not clear how the rotational and/or magnetic energy is transferred to the expanding ejecta. It might also be in the form of high-energy photons, in which case the leakage would occur in a similar way as in the radioactive decay model. We note that the initial spin period that we find ($P_{\text{sp,init}} = 2.30 \pm 0.03$ ms) is lower than that inferred by Chen et al. (2015, $P_{\text{sp,init}} = 2.72$ ms), which moves the location of PTF 12dam in the spin period vs. host-metallicity plot shown in Fig. 7 of Chen et al. (2016) slightly away from the suggested relation.

The energy input in the CSM interaction model originates from the SN ejecta interacting with dense CSM (e.g., a dense progenitor wind or circumstellar shell previously cast off by the progenitor), resulting in a forward/circumstellar and a reverse/ejecta shock. Chatzopoulos et al. (2013) use Chevalier (1982) and Chevalier & Fransson (1994) to derive an expression for the time-dependent luminosity produced by the forward and reverse shocks, which are depositing kinetic energy into the CSM and SN ejecta, respectively. This is combined with the prescription of radiative diffusion developed by

Table 6
CSM interaction best-fit parameters.^a

	PTF 12dam	iPTF 13dcc	DES 14X3taz ^b
$t_{\text{expl,rest}}$ [d]	-70 ^c	-79	-43 ^c
δ	0	2	2
n	8	6	14
s	0	0	0
R_{prog} [R_{\odot}]	0.1 ^c	0.1 ^c	0.1 ^c
ρ_{CSM} [10^{-13} g cm ⁻³]	5	0.3	4
M_{CSM} [M_{\odot}]	15	14	6
M_{ejecta} [M_{\odot}]	13	3	7
E_{SN} [10^{51} erg]	3	3	1
χ^2/DOF	1.8/31	41.9/49	16.4/8
$R_{\text{CSM}}^{\text{d}}$ [10^{15} cm]	2	6	2
$v_{\text{exp}}^{\text{d}}$ [10^3 km s ⁻¹]	15	25	15

^a Owing to the complexity of the model, these best-fit values are very uncertain and should be considered as rough approximations.

^b For DES 14X3taz the first two detections have been discarded in the fit, focussing on fitting the main peak.

^c Parameter reached limit of allowed range.

^d The lower two parameters are not fit, but are calculated within the model.

Arnett (1980, 1982) to derive an analytic expression for the output bolometric light curve (see Eq. 20 of Chatzopoulos et al. 2013). The model has many free parameters: the time of the explosion ($t_{\text{expl,rest}}$), the power-law index for the inner and outer ejecta density profile (δ and n , respectively), the power-law index for the CSM density profile (s), the progenitor radius (R_{prog}), the density immediately outside the progenitor envelope (ρ_{CSM}), the CSM mass (M_{CSM}), the ejecta mass (M_{ejecta}), and the total SN energy (E_{SN}). In our fitting routine, we loop over the following typical values for the parameters: $\delta = [0, 2]$, $n = 6\text{--}14$, and $s = [0, 2]$ ($s = 0$ signifies a constant CSM density profile, such as that of a shell of material, while $s = 2$ corresponds to that produced by a progenitor wind), and find the best-fit values for the remaining parameters. The best-fit values are listed in Table 6, and the corresponding best-fit model for PTF 12dam is shown by the solid red line in Fig. 7.

The CSM interaction model provides an excellent fit to the data ($\chi_{\nu}^2 = 0.1$), but considering the number of free parameters, this may not be so surprising (see also Chatzopoulos et al. 2013). This CSM interaction model can be combined with the model for radioactive decay of nickel and cobalt, adding another free parameter, the nickel mass (M_{Ni}), but we fixed this to zero in the CSM fit.

We also fit the analytic shock-cooling model of an extended envelope surrounding the SN developed by Nakar & Piro (2014) and Piro (2015) to the observed early-time r -band light curve of PTF 12dam. The parameters are the time of the explosion (t_{expl}), the core mass (M_{core}), the energy in the SN shock (which is transferred to the extended material, E_{SN}), and the mass, radius, and opacity of the extended material (M_{ext} , R_{ext} , and κ , respectively). The term M_{core} is somewhat misleading; it refers to the part of the original stellar core that is ejected, i.e. the mass of the core minus the mass of the stellar remnant (see Nakar & Piro 2014). We fix $\kappa = 0.2$ cm² g⁻¹ as for all the other models. We limit the SN energy and extended radius to be at most $E_{\text{SN}} \leq 10^{53}$ erg and $R_{\text{ext}} \leq 10^{14}$ cm, respectively. The extended mass is con-

Table 7
Piro (2015) best-fit parameters.^a

	PTF 12dam	iPTF 13dcc	DES 14X3taz
$t_{\text{expl,rest}}$ [d]	-75 ^b	-70 ^b	-45
M_{core} [M_{\odot}]	1 ^b	35	4
E_{SN} [10^{51} erg]	3 ^c	100 ^b	1 ^c
M_{ext} [M_{\odot}]	0.5 ^b	17.5 ^b	0.4
R_{ext} [10^{13} cm]	0.6	10 ^b	10 ^c
χ^2/DOF	3.0/2	52.7/17	0.004/1

^a Owing to the degeneracy of the parameters in this model, these best-fit values are very uncertain and should be considered as rough approximations.

^b Parameter reached limit of allowed range.

^c Parameter was held fixed; in the case of PTF 12dam and DES 14X3taz the explosion energy was fixed to the same value as the best-fit value of the CSM interaction model (see Table 6).

strained to be at most half the core mass, and the latter is required to be at least 1 M_{\odot} . Given these parameters, the time evolution of the bolometric luminosity and radius of the extended material is provided by the model.

To fit the model to the observed magnitudes, we determine the effective temperature evolution based on the model parameters and transform the resulting rest-frame spectral blackbody flux to the observer’s frame. We then extract observed model magnitudes by performing synthetic photometry on the spectrum using the P48 r -band transmission curve. To make use of the r -band upper limits nearest in time to the first detections, we converted the limits at an observed time of about -73 and -76 days to expectation values of half the limit, with an uncertainty (1σ) the size of one sixth of the limit, so these added data points are consistent with the 3σ upper limit. We did the same for the measurement at an observed time around -63 days, as by this time the luminosity is already dominated by whatever is powering the main peak. Although this is not clear in Fig. 1, the r -band measurement at an observed time of -70 days is in fact composed of three different data points; hence, in the fit we use a total of seven measurements. Even when making use of the limits in the fit, the number of data points is limited. We therefore decided to fix the explosion energy to the best-fit value found for the CSM interaction fit. The resulting best-fit values are listed in Table 7. This fit is shown by the red solid line in the inset of Fig. 1. As already noted, the number of degrees of freedom is very low (two), and so the parameters are not well constrained. However, this is just to show that the Piro model is capable of explaining the early-time evolution of the PTF 12dam light-curve with reasonable values for the parameters. For LSQ 14bdq, Piro (2015) find acceptable fits with the following ranges of values for the fit parameters: $M_{\text{ext}} = 0.3\text{--}0.5 M_{\odot}$, $R_{\text{ext}} = 500\text{--}5000 R_{\odot}$ ($= 3.5 \times 10^{13\text{--}14}$ cm), and $E_{\text{SN}} = (9\text{--}55) \times 10^{51}$ erg.

4.2. iPTF 13dcc

Figure 8 shows the bolometric light curve of iPTF 13dcc as derived in Sec. 3. As we did for PTF 12dam, we fit the Chatzopoulos and Piro models to our light-curve data. Again, we adopt a Thomson electron scattering opacity of $\kappa = 0.2$ cm² g⁻¹ and for iPTF 13dcc we assume that the time of explosion is in the phase range of -100 to -70 days. We loosely limit

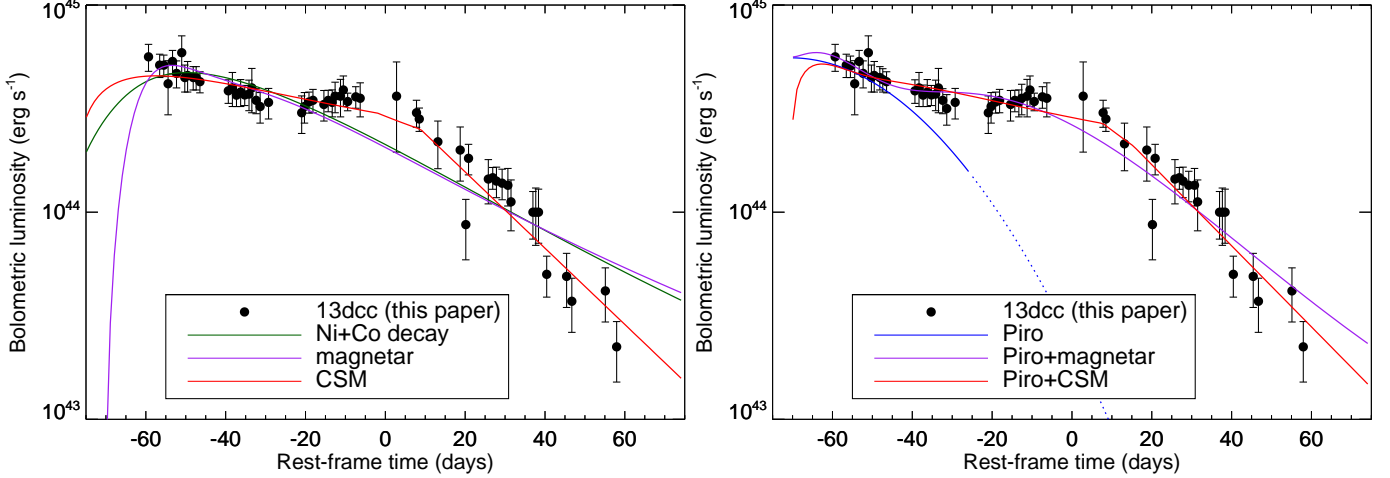


Figure 8. Left panel: model fits of radioactive decay, magnetar, and CSM interaction to the bolometric light curve of iPTF 13dcc (up to a phase of +80 days). While the radioactive decay and magnetar models fail to fit both the early excess emission and main peak, the CSM interaction model describes the observations rather well. Right panel: a Piro model fit to the early-time light curve (phase < -25 days), and a combination of the Piro plus magnetar and Piro plus CSM interaction models to the iPTF 13dcc light curve. The two breaks in the CSM interaction model light curve, seen in both panels, correspond to the times of termination of the forward and reverse shocks. See Tables 4-9 for the corresponding parameter best-fit values for all these model fits.

Table 8
Piro+magnetar best-fit parameters.^a

	iPTF 13dcc	DES 14X3taz
$t_{\text{expl,rest}}$ [d]	-70 ^b	-43 ^b
M_{core} [M_{\odot}]	12	1.2
M_{ext} [M_{\odot}]	6	0.6 ^b
R_{ext} [10^{13} cm]	4	0.2
E_{SN} [10^{51} erg]	100 ^b	20
$P_{\text{sp,init}}$ [ms]	1.2 ± 1.7	1.8 ± 2.8
B_{14} [10^{14} G]	1.1 ± 0.8	0.4 ± 0.7
t_{d} [d]	66 ± 72	49 ± 209
A_{leakage} [10^3 d ²]	11 ± 37	3 ± 11
R_0 [R_{\odot}]	0.1 ^b	0.1 ^b
χ^2/DOF	48.9/46	34.2/7

^a Owing to the degeneracy of the Piro parameters in this model, these Piro-model best-fit values are very uncertain and should be considered as rough approximations.

^b Parameter reached limit of allowed range.

Table 9
Piro+CSM interaction best-fit parameters.^a

	iPTF 13dcc ^a	DES 14X3taz
$t_{\text{expl,rest}}$ [d]	-70 ^b	-43 ^b
M_{core} [M_{\odot}]	2.4	7.9
M_{ext} [M_{\odot}]	1.2 ^b	0.1
R_{ext} [10^{13} cm]	10 ^b	7
δ	2	0
n	6	14
s	0	0
R_{prog} [R_{\odot}]	0.4	0.1 ^b
ρ_{CSM} ^c [10^{-13} g cm ⁻³]	0.3	5
M_{CSM} [M_{\odot}]	12	6
M_{ejecta} [M_{\odot}]	3.6	8.0
E_{SN} [10^{51} erg]	3	2
χ^2/DOF	36.6/47	16.6/8
R_{CSM} ^c [10^{15} cm]	6	2
v_{exp} ^c [10^3 km s ⁻¹]	23	18

^a Owing to the complexity of the model, these best-fit values are very uncertain and should be considered as rough approximations.

^b Parameter reached limit of allowed range.

^c The lower two parameters are not fit, but are calculated within the CSM interaction model.

the radius of the progenitor star, R_0 , to be within the range 0.1–500 R_{\odot} , and use a fiducial value for the expansion velocity of 10,000 km s⁻¹ for the radioactive decay and magnetar models. The resulting best-fit values for the model parameters of the radioactive decay, magnetar, and CSM interaction models are listed in Tables 4, 5, and 6, respectively; the corresponding model fits are shown in the left panel of Fig. 8. The amount of nickel required to power iPTF 13dcc is very large (albeit with an even larger formal uncertainty), much larger than the calculated mass in the ejecta ($M_{\text{ej}} \approx 15 M_{\odot}$), rendering this model unphysical. Also, the magnetar model is unable to describe both the early emission and “main” peak.

We also fit the analytic shock-cooling model of Piro (2015) to the bolometric light curve of iPTF 13dcc. As for PTF 12dam, we limit the SN energy and extended radius to be at most $E_{\text{SN}} \leq 10^{53}$ erg and $R_{\text{ext}} \leq 10^{14}$ cm, respectively, and the extended mass is constrained to be at most half the core mass. The best-fit values are given in Table 7 and the best fit is shown in the right panel of

Fig. 8. The line turns from solid to dotted at a phase of -25 days, beyond which the data points were excluded in this fit. The fit is good at early times, but undershoots the data points between a phase of -45 and -25 days. A larger explosion energy of 1.5×10^{53} erg would provide a very good fit, but this is unreasonably high. The inferred extended mass, which is the main parameter determining the light-curve width, is much larger in the case of iPTF 13dcc ($\sim 18 M_{\odot}$) than that needed to explain the excess emission in PTF 12dam ($\sim 0.5 M_{\odot}$).

Finally, we fit a combination of the Piro plus magnetar and also Piro plus CSM interaction to the iPTF 13dcc observations. In the latter combined model, the explosion energy is set to the same value in both the Piro and CSM interaction models, and the ejecta mass (of the CSM interaction model) set to the sum of the core mass and the extended mass (both of the Piro model):

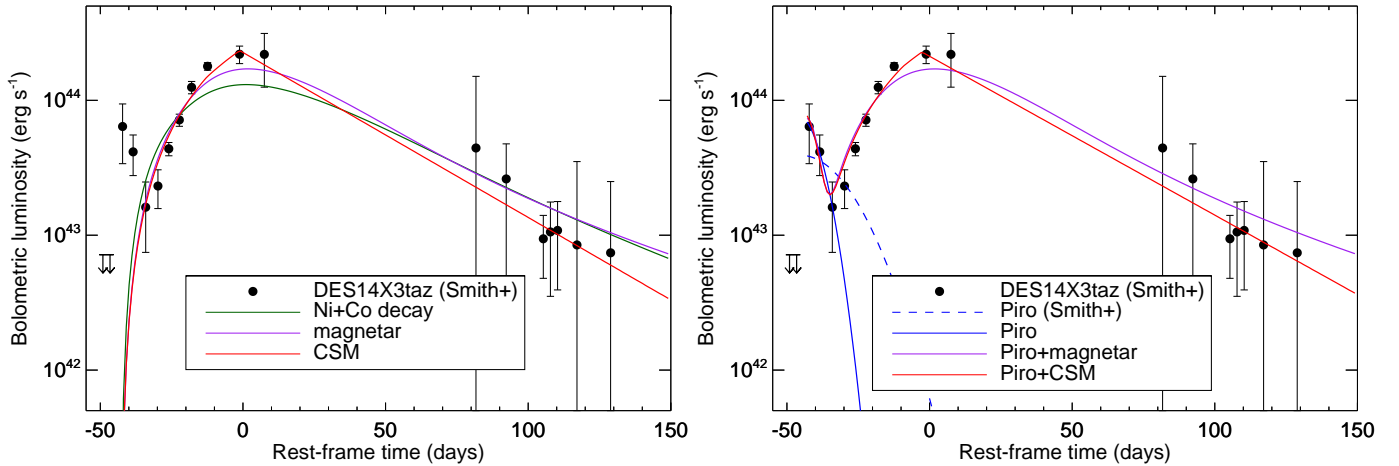


Figure 9. Model fits of radioactive decay, magnetar, CSM interaction, and the Piro model to the bolometric light curve of DES 14X3taz (Smith et al. 2016). In the left panel, we only fit the main peak, and the first two detections have been excluded in the fits. The radioactive decay model provides a poor fit, while the magnetar model fits the data reasonably well. The CSM interaction model provides the best match with the observations. On the right, we fit the Piro (2015) model to the first three detections, indicated with the solid blue line. For reference, we also show the model parameters found by Smith et al. (2016) from fitting the *griz* magnitudes rather than the bolometric luminosity as we do in this paper. We also perform combined Piro+magnetar and Piro+CSM interaction fits, shown by the solid lines in the right panel. See Tables 4–9 for the corresponding parameter best-fit values for all these model fits.

$M_{\text{core}} + M_{\text{ext}} = M_{\text{ejecta}}$. This is because the ejected core mass is sweeping up the extended mass, which is at a lower distance than the CSM mass, and thus the sum of these masses equals the ejecta mass in the CSM interaction model. The best-fit parameters of these combination models are listed in Tables 8 and 9, and the corresponding light curves are shown in the right panel of Fig. 8.

4.3. DES 14X3taz

Smith et al. (2016) present observations of the hydrogen-poor SLSN DES 14X3taz, which also shows evidence for early-time excess emission. These authors were able to catch this early emission in multiple filters, for the first time, allowing for a quite accurate determination of the temperature, radius, and bolometric light-curve evolution for the early-time emission. Since the bolometric evolution of this SLSN is so well constrained from a very early epoch, we also fit DES 14X3taz with the same models as we have done for PTF 12dam and iPTF 13dcc above. The filled black circles in Fig. 9 show the bolometric light curve of DES 14X3taz as presented by Smith et al. (2016). The time of explosion for DES 14X3taz is very well constrained by observations to be in the range -50 to -43 days. As for PTF 12dam and iPTF 13dcc, we loosely limit the radius of the progenitor star, R_0 , to be within the range 0.1 – $500 R_{\odot}$, and use a fiducial value for the expansion velocity of $10,000 \text{ km s}^{-1}$. We exclude the first two detections and focus on fitting the models to the main peak, but constraining the time of explosion to be before the first detection. The resulting best-fit values for the model parameters of the radioactive decay, magnetar, and CSM interaction models are listed in Tables 4, 5, and 6, respectively. The corresponding bolometric-luminosity evolution is shown in the left panel of Fig. 9. As we did for iPTF 13dcc in the previous section, a combination of the Piro plus magnetar and Piro plus CSM interaction models is fit to the full light curve of DES 14X3taz. The best-fit parameters of these combination models are listed alongside those of iPTF 13dcc in Tables 8 and 9, and the corresponding bolometric model light curves are shown in the right panel of Fig. 9.

5. DISCUSSION

Figure 10 shows a comparison of the absolute *g*-band light curves of iPTF 13dcc, LSQ 14bdq, SN 2006oz, DES 14X3taz, and PTF 12dam. The iPTF 13dcc data were derived by converting the observed *r*-band measurements to rest-frame *g*, where we computed the K-corrections adopting the temperature evolution of PTF 12dam (see Fig. 6). Since the effective wavelengths of the observed *r*-band and rest-frame *g*-band filters match well at the redshift of iPTF 13dcc ($z = 0.431$), these K-corrections are very close to $-2.5 \log(1+z)$ and do not depend very much on the assumed temperature evolution. For PTF 12dam ($z = 0.107$), we instead computed a continuous rest-frame *g*-band light curve by adopting the temperature and bolometric luminosity evolution as derived in Fig. 3. For each SLSN shown in Fig. 10, except for iPTF 13dcc, we shifted the PTF 12dam light curve, in both time and magnitude, to match the data points. This is simply to show how the observed early excess emission of each SLSN compares in duration and magnitude with that of the others. For both SN 2006oz and DES 14X3taz the match with PTF 12dam at early epochs is quite good, whereas at late times the DES 14X3taz light curve is dropping much more rapidly than that of PTF 12dam. For LSQ 14bdq the early excess emission is longer and brighter than that of PTF 12dam, but at late times the two match surprisingly well. The obvious outlier is the light curve of iPTF 13dcc: its early emission is of a much longer duration and a few magnitudes brighter than those of the others.

Kasen et al. (2016) suggest that the early excess emission observed for LSQ 14bdq could be caused by a magnetar central engine whose energy input drives a shock through the pre-exploded SN ejecta, resulting in a burst of shock-breakout emission several days after the explosion. The radiation is expected to be released in the optical/UV wavelengths and to have a duration of several days, with the emission being dimmer than the main light-curve peak resulting from continued magnetar heat-

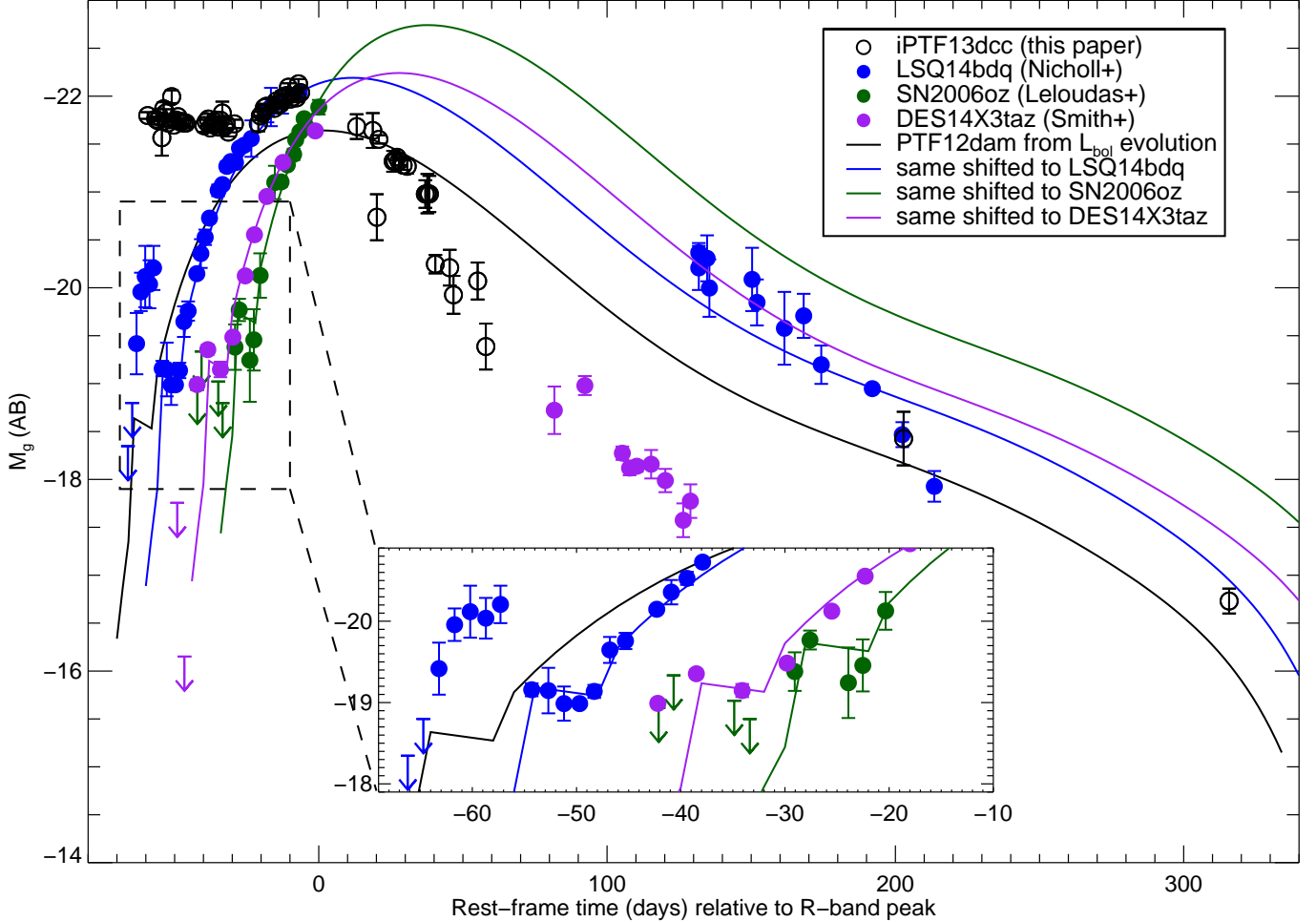


Figure 10. Absolute g -band light curves of iPTF 13dcc (open black circles), LSQ14bdq (filled blue circles; Nicholl et al. 2015), SN 2006oz (filled green circles; Leloudas et al. 2012), and DES 14X3taz (filled purple circles; Smith et al. 2016). The solid black line shows the PTF 12dam evolution assuming the temperature and radius evolution as inferred from the photometry and as shown in Fig. 3. The blue, green, and purple lines correspond to the PTF 12dam M_g light curve simply shifted in time and magnitude to roughly match the data points of LSQ14bdq, SN 2006oz, and DES 14X3taz, respectively. The open black circles are the iPTF 13dcc M_g values inferred from the observed P48 and P60 r -band magnitudes, applying a K-correction that is based on the temperature evolution of PTF 12dam (see Fig. 6).

ing. As can be seen in Fig. 7 of Kasen et al. (2016), for standard magnetar and ejecta parameters, the shock-breakout emission produces only a kink in the overall light curve. In principle, this model is capable of explaining the early excess emission in PTF 12dam. However, the early emission that we observe for iPTF 13dcc is too bright and too extended to be accommodated in this model. Even when pushing the ejecta mass and kinetic energy to large values (see Fig. 8 of Kasen et al. 2016), this model is not able to reproduce the iPTF 13dcc observations.

Based on the model fits presented in Sec. 4, the CSM interaction model seems to provide better fits to the data. Moreover, the magnetar model is unable by itself to fit the precursor bumps seen in SLSNe but requires the addition of the Piro model (or similar) and the presence of extended material at large radii to explain the first peak. The combination of Piro and magnetar provides a reasonable description of the iPTF 13dcc light curve, even though it does not fit the data well around peak and appears to overshoot the data beyond +40 days. Moreover, the explosion energy for this model reaches the upper end of the range that we allowed: $E_{\text{SN}} = 10^{53}$ erg. We find

that the CSM interaction model, which in fact contains one free parameter less than the number used in the combined Piro and magnetar model, can provide a good fit to the iPTF 13dcc light curve, even without the addition of the Piro model (see Table 6 and Fig. 8). The first minimum in the light curve cannot be accurately reproduced (see the left panel of Fig. 8), but a time-dependent opacity (we have assumed a constant opacity throughout this paper) could be invoked to explain the early light-curve shape. Also, this iPTF 13dcc light-curve dip is reminiscent of the picture proposed by Moriya & Maeda (2012), where a drop in the light curve arises naturally. These authors suggest that such a dip is a solid prediction from the strong interaction scenario regardless of the power source for the early emission.

The ability of the CSM interaction model to reproduce the light curves of many SLSNe can be explained by the fact that it includes many free parameters. In addition, the CSM model by Chatzopoulos et al. (2012, 2013) includes a number of simplifying assumptions of which the most important are those of a central power source and a stationary photosphere, allowing for the use of Arnett-style diffusion by using analytical equations. However, it

is not clear if these assumptions hold in real CSM interaction. Chatzopoulos et al. verify their model against a more sophisticated hydrodynamical model developed for the H-rich SN 2006gy (Moriya et al. 2013) and obtain a reassuringly similar light curve for similar parameters. Extending the use of the model to H-poor SLSNe, such as PTF 12dam and iPTF 13dcc, is not trivial, however, owing to the different treatment of the opacity when hydrogen is absent. Nevertheless, models that successfully reproduce the light curves of H-poor SLSNe by using CSM interaction have now been reproduced in radiation hydrodynamics simulations by Sorokina et al. (2016), although these authors do report discrepancies in some parameters of their models in comparison to those obtained with the Chatzopoulos models for the same SLSNe. The CSM interaction semi-analytical models remain a valuable tool, and it is clear that H-poor CSM interaction can reproduce the light curves of SLSNe, more naturally explaining features such as premaximum bumps in a self-consistent way. However, these caveats show that caution should be used in interpreting the best-fit model parameters based on χ^2 minimization of the semi-analytical CSM interaction models.

On a final note, an argument often invoked against the CSM interaction model for hydrogen-poor SLSNe is the lack of narrow emission lines, as observed for Type II_n SNe. However, to date, the spectroscopic signature(s) of interaction with a H-deficient dense CSM has not been investigated through spectral synthesis modelling, due to its complexity.

It is a pleasure to acknowledge the help of Manos Chatzopoulos with the implementation of the semi-analytical light-curve models developed by him and his colleagues in our light-curve fitting program. We are grateful to Nir Sapir for enlightening discussions, and to WeiKang Zheng, Kelsey Clubb and Patrick Kelly for their contribution to the 2013 Dec. 3 Keck/LRIS observations of iPTF 13dcc. We thank the staffs at Palomar and Lick Observatories for their expert assistance. The intermediate Palomar Transient Factory project is a scientific collaboration among the California Institute of Technology, Los Alamos National Laboratory, the University of Wisconsin at Milwaukee, the Oskar Klein Center, the Weizmann Institute of Science, the TANGO Program of the University System of Taiwan, and the Kavli Institute for the Physics and Mathematics of the Universe. This paper is based in part on observations made with the NASA/ESA *Hubble Space Telescope*. Some of the data presented herein were obtained at the W.M. Keck Observatory, which is operated as a scientific partnership among the California Institute of Technology, the University of California, and NASA; the observatory was made possible by the generous financial support of the W.M. Keck Foundation. Research at Lick Observatory is partially supported by a generous gift from Google. These results also made use of the Discovery Channel Telescope at Lowell Observatory. Lowell is a private, non-profit institution dedicated to astrophysical research and public appreciation of astronomy and operates the DCT in partnership with Boston University, the University of Maryland, the University of Toledo, Northern Arizona University and Yale University. LMI construction was

Table 10
Log of observations of PTF 12dam.

MJD (days)	Phase ^a (days)	Telescope	Filter	Magnitude ^b AB
56009.34	-78.92	P48	R	> 22.26
56013.35	-75.30	P48	R	> 22.10
56017.29	-71.73	P48	R	> 22.13
56020.41	-68.91	P48	R	> 21.94
56023.28	-66.33	P48	R	> 20.69
56025.33	-64.47	P48	R	20.11 ± 0.17
56027.26	-62.73	P48	R	20.02 ± 0.12
56027.29	-62.70	P48	R	20.11 ± 0.11
56027.32	-62.68	P48	R	20.04 ± 0.10
56033.49	-57.10	P48	R	19.89 ± 0.08
56034.16	-56.49	P48	R	19.96 ± 0.08
56034.19	-56.46	P48	R	19.96 ± 0.08
56034.26	-56.41	P48	R	19.83 ± 0.07
56036.17	-54.68	P48	R	19.77 ± 0.08
56036.21	-54.64	P48	R	19.68 ± 0.07
56036.37	-54.50	P48	R	19.70 ± 0.07
56038.35	-52.71	P48	R	19.37 ± 0.04
56038.38	-52.69	P48	R	19.39 ± 0.04
56040.43	-50.83	P48	R	19.28 ± 0.04
56040.46	-50.81	P48	R	19.22 ± 0.04
56046.40	-45.44	P48	R	18.55 ± 0.03
56046.43	-45.41	P48	R	18.57 ± 0.03
56048.43	-43.60	P48	R	18.34 ± 0.03
56048.47	-43.57	P48	R	18.43 ± 0.02
56048.50	-43.54	P48	R	18.36 ± 0.03
56058.47	-34.53	P48	R	17.76 ± 0.02
56059.28	-33.81	P48	R	17.69 ± 0.01
56061.33	-31.95	P48	R	17.64 ± 0.01
56063.29	-30.18	P48	R	17.53 ± 0.01
56063.32	-30.15	P48	R	17.51 ± 0.01
56063.35	-30.12	P48	R	17.57 ± 0.01
56065.44	-28.24	P48	R	17.46 ± 0.02
56066.38	-27.39	P48	R	17.44 ± 0.01
56066.41	-27.36	P48	R	17.46 ± 0.01
56066.45	-27.33	P48	R	17.44 ± 0.01
56068.48	-25.50	P48	R	17.38 ± 0.01
56070.40	-23.76	P48	R	17.28 ± 0.01
56070.44	-23.73	P48	R	17.28 ± 0.01
56070.47	-23.70	P48	R	17.29 ± 0.01
56076.37	-18.36	P48	R	17.12 ± 0.01
56076.40	-18.33	P48	R	17.16 ± 0.01
56362.48	240.09	P48	R	20.70 ± 0.13
56362.51	240.12	P48	R	20.42 ± 0.10
56362.54	240.14	P48	R	20.59 ± 0.13
56366.49	243.71	P48	R	20.40 ± 0.17
56366.50	243.72	P48	R	20.56 ± 0.10
56366.51	243.73	P48	R	20.78 ± 0.13
56366.52	243.74	P48	R	20.60 ± 0.11
56369.54	246.47	P48	R	20.51 ± 0.13
56374.51	250.96	P48	R	20.48 ± 0.12
56376.51	252.76	P48	R	21.01 ± 0.20
56385.51	260.90	P48	R	20.48 ± 0.27
56068.22	-25.73	P60	i	17.52 ± 0.01
56068.22	-25.73	P60	r	17.42 ± 0.01
56068.22	-25.73	P60	B	17.14 ± 0.01
56068.22	-25.72	P60	g	17.13 ± 0.01
56068.23	-25.72	P60	i	17.54 ± 0.01
56068.23	-25.72	P60	r	17.34 ± 0.01
56068.23	-25.72	P60	B	17.21 ± 0.01
56068.23	-25.72	P60	g	17.13 ± 0.01
56075.23	-19.39	P60	i	17.31 ± 0.01
56075.24	-19.39	P60	r	17.22 ± 0.01
56075.24	-19.39	P60	B	16.80 ± 0.01
56075.24	-19.39	P60	g	17.17 ± 0.01
56080.20	-14.90	P60	i	17.19 ± 0.01
56080.20	-14.90	P60	r	17.02 ± 0.01
56080.20	-14.90	P60	B	16.87 ± 0.01
56080.21	-14.90	P60	g	16.82 ± 0.01
56080.21	-14.90	P60	i	17.19 ± 0.01
56080.21	-14.90	P60	r	17.05 ± 0.01
56080.21	-14.90	P60	B	16.90 ± 0.01
56080.21	-14.89	P60	g	16.76 ± 0.01

^a Calculated using $MJD_{r,peak} = 56096.7$ and $z = 0.107$.

^b The magnitudes have *not* been corrected for Galactic extinction.

Table 10
(continued) Log of observations of PTF 12dam.

MJD (days)	Phase ^a (days)	Telescope	Filter	Magnitude ^b AB
56085.21	-10.38	P60	i	17.11 ± 0.01
56085.21	-10.38	P60	r	16.98 ± 0.01
56085.21	-10.38	P60	B	16.83 ± 0.01
56085.21	-10.38	P60	i	17.21 ± 0.01
56085.21	-10.38	P60	r	17.05 ± 0.01
56085.21	-10.37	P60	B	16.83 ± 0.01
56085.22	-10.37	P60	g	16.78 ± 0.01
56090.20	-5.87	P60	i	17.05 ± 0.01
56090.20	-5.87	P60	r	16.92 ± 0.01
56090.20	-5.87	P60	g	16.74 ± 0.01
56090.20	-5.87	P60	i	17.19 ± 0.01
56090.21	-5.87	P60	r	16.91 ± 0.01
56090.21	-5.87	P60	B	16.89 ± 0.01
56090.22	-5.85	P60	g	16.78 ± 0.01
56098.29	1.44	P60	i	17.10 ± 0.01
56098.29	1.44	P60	r	16.98 ± 0.01
56098.29	1.44	P60	B	16.90 ± 0.01
56098.30	1.44	P60	i	17.12 ± 0.01
56098.30	1.44	P60	r	16.95 ± 0.01
56098.30	1.44	P60	B	16.89 ± 0.01
56098.30	1.44	P60	g	16.78 ± 0.01
56103.21	5.88	P60	i	17.08 ± 0.01
56103.21	5.88	P60	r	16.96 ± 0.01
56103.22	5.89	P60	g	16.97 ± 0.01
56103.22	5.89	P60	i	17.13 ± 0.01
56103.23	5.90	P60	r	17.12 ± 0.01
56103.23	5.90	P60	B	16.86 ± 0.01
56103.23	5.90	P60	g	16.84 ± 0.01
56108.21	10.40	P60	i	17.11 ± 0.01
56108.21	10.40	P60	r	17.02 ± 0.01
56108.21	10.40	P60	B	17.00 ± 0.01
56108.21	10.40	P60	g	16.80 ± 0.01
56108.21	10.40	P60	i	17.12 ± 0.01
56108.21	10.40	P60	r	17.02 ± 0.01
56108.21	10.40	P60	B	16.99 ± 0.01
56108.21	10.40	P60	g	16.87 ± 0.01
56113.20	14.91	P60	i	17.13 ± 0.01
56113.20	14.91	P60	r	17.09 ± 0.01
56113.20	14.91	P60	B	17.08 ± 0.02
56113.21	14.91	P60	g	16.86 ± 0.01
56113.21	14.91	P60	i	17.15 ± 0.01
56113.21	14.91	P60	r	17.02 ± 0.01
56113.21	14.91	P60	B	17.10 ± 0.02
56113.21	14.91	P60	g	16.89 ± 0.01
56118.25	19.47	P60	i	17.17 ± 0.01
56118.25	19.47	P60	r	17.11 ± 0.01
56118.25	19.47	P60	B	17.18 ± 0.01
56118.25	19.47	P60	g	16.99 ± 0.01
56118.26	19.47	P60	i	17.21 ± 0.01
56118.26	19.47	P60	r	17.08 ± 0.01
56118.26	19.47	P60	B	17.16 ± 0.01
56118.26	19.48	P60	g	16.99 ± 0.01
56127.28	27.62	P60	g	17.47 ± 0.02
56129.20	29.36	P60	i	17.37 ± 0.01
56129.20	29.36	P60	r	17.24 ± 0.01
56129.20	29.36	P60	B	17.41 ± 0.01
56129.20	29.36	P60	g	17.22 ± 0.01
56159.20	56.46	P60	i	17.62 ± 0.02
56161.18	58.24	P60	r	17.56 ± 0.01
56161.18	58.24	P60	B	18.11 ± 0.02
56161.18	58.25	P60	g	17.87 ± 0.01
56165.17	61.85	P60	i	17.54 ± 0.02
56177.15	72.67	P60	i	17.67 ± 0.02
56177.15	72.67	P60	r	17.78 ± 0.01
56177.15	72.67	P60	B	18.46 ± 0.03
56177.15	72.67	P60	g	17.98 ± 0.01
56185.16	79.91	P60	i	17.90 ± 0.02
56185.16	79.91	P60	r	17.92 ± 0.02
56185.16	79.91	P60	B	18.54 ± 0.03
56185.16	79.91	P60	g	18.18 ± 0.02
56185.17	79.91	P60	i	17.80 ± 0.02
56185.17	79.92	P60	r	17.92 ± 0.02

^a Calculated using $\text{MJD}_{r,\text{peak}} = 56096.7$ and $z = 0.107$.

^b The magnitudes have *not* been corrected for Galactic extinction.

Table 10
(continued) Log of observations of PTF 12dam.

MJD (days)	Phase ^a (days)	Telescope	Filter	Magnitude ^b AB
56185.17	79.92	P60	B	18.59 ± 0.04
56185.17	79.92	P60	g	18.15 ± 0.02
56201.11	94.32	P60	g	18.46 ± 0.03
56202.11	95.22	P60	i	17.92 ± 0.02
56202.11	95.22	P60	r	18.15 ± 0.02
56214.10	106.05	P60	i	18.30 ± 0.03
56214.10	106.06	P60	r	18.31 ± 0.02
56214.10	106.06	P60	B	19.09 ± 0.04
56214.11	106.06	P60	g	18.58 ± 0.02
56237.55	127.23	P60	i	18.73 ± 0.06
56245.54	134.45	P60	i	18.73 ± 0.13
56245.54	134.45	P60	B	19.84 ± 0.18
56245.54	134.45	P60	g	19.29 ± 0.09
56250.51	138.95	P60	r	19.21 ± 0.04
56251.51	139.85	P60	r	19.17 ± 0.03
56252.51	140.75	P60	i	19.10 ± 0.05
56252.51	140.75	P60	B	19.97 ± 0.11
56252.51	140.75	P60	g	19.59 ± 0.05
56262.54	149.81	P60	r	19.42 ± 0.09
56265.48	152.46	P60	g	19.56 ± 0.21
56266.47	153.36	P60	r	19.16 ± 0.04
56266.47	153.36	P60	g	19.62 ± 0.07
56268.47	155.16	P60	B	20.11 ± 0.10
56273.45	159.67	P60	r	19.53 ± 0.05
56273.45	159.67	P60	g	19.86 ± 0.06
56281.43	166.87	P60	i	19.64 ± 0.15
56281.43	166.88	P60	r	19.50 ± 0.09
56283.43	168.68	P60	r	19.55 ± 0.03
56283.43	168.68	P60	B	20.21 ± 0.09
56283.43	168.68	P60	g	19.84 ± 0.05
56297.39	181.29	P60	i	19.66 ± 0.07
56297.39	181.29	P60	r	19.67 ± 0.04
56297.39	181.29	P60	B	20.13 ± 0.10
56297.39	181.29	P60	g	20.00 ± 0.06
56323.31	204.71	P60	i	20.03 ± 0.13
56323.32	204.71	P60	r	20.45 ± 0.15
56323.32	204.71	P60	g	20.39 ± 0.16
56324.31	205.61	P60	r	20.30 ± 0.07
56345.33	224.60	P60	i	20.18 ± 0.13
56345.34	224.60	P60	r	20.41 ± 0.11
56345.34	224.61	P60	B	20.75 ± 0.27
56345.34	224.61	P60	g	20.83 ± 0.16
56345.34	224.61	P60	i	20.22 ± 0.12
56345.34	224.61	P60	r	20.36 ± 0.10
56345.35	224.61	P60	B	20.63 ± 0.24
56345.35	224.61	P60	g	20.61 ± 0.13
56346.25	225.43	P60	i	20.55 ± 0.20
56346.25	225.43	P60	r	20.18 ± 0.12
56346.26	225.44	P60	g	20.43 ± 0.17
56347.43	226.50	P60	i	20.17 ± 0.21
56347.43	226.50	P60	r	20.59 ± 0.22
56347.44	226.50	P60	g	20.62 ± 0.26
56349.24	228.13	P60	i	19.78 ± 0.21
56350.24	229.04	P60	r	20.49 ± 0.25
56350.25	229.04	P60	g	20.55 ± 0.31
56352.24	230.84	P60	r	20.47 ± 0.16
56352.24	230.84	P60	g	20.90 ± 0.28
56353.23	231.74	P60	r	20.46 ± 0.09
56353.24	231.74	P60	B	21.23 ± 0.26
56353.24	231.74	P60	g	20.62 ± 0.10
56356.23	234.44	P60	i	20.44 ± 0.12
56362.27	239.90	P60	r	20.55 ± 0.09
56362.28	239.91	P60	B	21.01 ± 0.21
56362.28	239.91	P60	g	20.82 ± 0.10
56362.28	239.91	P60	r	20.56 ± 0.09
56362.28	239.91	P60	B	20.97 ± 0.19
56362.28	239.91	P60	g	20.82 ± 0.10
56364.20	241.65	P60	i	20.25 ± 0.09
56370.31	247.16	P60	r	20.70 ± 0.13
56370.31	247.16	P60	B	20.84 ± 0.23
56371.25	248.01	P60	g	21.28 ± 0.29
56372.20	248.87	P60	r	20.44 ± 0.22

^a Calculated using $\text{MJD}_{r,\text{peak}} = 56096.7$ and $z = 0.107$.

^b The magnitudes have *not* been corrected for Galactic extinction.

Table 10
(continued) Log of observations of PTF 12dam.

MJD (days)	Phase ^a (days)	Telescope	Filter	Magnitude ^b AB
56373.18	249.76	P60	i	20.71 ± 0.25
56373.18	249.76	P60	r	20.51 ± 0.21
56374.18	250.66	P60	r	20.20 ± 0.25
56375.29	251.66	P60	i	20.64 ± 0.14
56375.29	251.66	P60	r	21.33 ± 0.18
56375.29	251.67	P60	g	21.01 ± 0.09
56376.17	252.46	P60	r	20.89 ± 0.25
56382.17	257.88	P60	B	21.04 ± 0.21
56386.17	261.49	P60	g	21.25 ± 0.13
56388.50	263.59	P60	r	21.19 ± 0.24
56388.50	263.59	P60	g	21.37 ± 0.15
56390.28	265.20	P60	r	20.72 ± 0.23
56392.27	267.00	P60	r	21.20 ± 0.26
56409.27	282.36	P60	i	20.78 ± 0.19
56412.46	285.24	P60	i	21.50 ± 0.24
56413.45	286.13	P60	r	21.58 ± 0.26
56416.39	288.79	P60	r	21.91 ± 0.30
56416.40	288.79	P60	g	21.92 ± 0.17
56422.43	294.25	P60	i	21.36 ± 0.20
56422.44	294.25	P60	g	22.35 ± 0.28
56425.34	296.88	P60	r	21.94 ± 0.27
56431.39	302.34	P60	i	21.40 ± 0.25
56432.32	303.18	P60	i	21.57 ± 0.23
56452.32	321.25	P60	r	21.97 ± 0.29
56459.24	327.50	P60	i	21.37 ± 0.18
56460.29	328.45	P60	i	21.45 ± 0.28
56470.27	337.46	P60	i	21.83 ± 0.31
56471.21	338.31	P60	r	22.19 ± 0.25
56507.22	370.84	P60	r	22.10 ± 0.23
56070.26	-23.88	LCOGT	r	17.23 ± 0.02
56070.26	-23.88	LCOGT	r	17.22 ± 0.02
56083.36	-12.05	LCOGT	r	17.00 ± 0.02
56086.44	-9.26	LCOGT	r	16.91 ± 0.02
56086.45	-9.26	LCOGT	r	16.94 ± 0.02
56089.33	-6.65	LCOGT	r	16.89 ± 0.02
56089.34	-6.65	LCOGT	r	16.90 ± 0.02
56128.38	28.62	LCOGT	r	17.20 ± 0.02
56128.38	28.62	LCOGT	r	17.22 ± 0.03
56149.24	47.47	LCOGT	r	17.41 ± 0.02
56149.25	47.47	LCOGT	r	17.42 ± 0.01
56152.24	50.17	LCOGT	r	17.48 ± 0.02
56152.24	50.17	LCOGT	r	17.46 ± 0.03
56156.24	53.79	LCOGT	r	17.55 ± 0.01
56156.24	53.79	LCOGT	r	17.62 ± 0.02
56181.23	76.36	LCOGT	r	17.87 ± 0.04
56181.23	76.36	LCOGT	r	17.91 ± 0.03
56187.24	81.79	LCOGT	r	17.97 ± 0.02
56196.21	89.90	LCOGT	r	18.18 ± 0.02
56196.22	89.90	LCOGT	r	18.03 ± 0.03
56197.22	90.81	LCOGT	r	18.11 ± 0.02
56197.22	90.81	LCOGT	r	18.23 ± 0.02
56200.21	93.51	LCOGT	r	18.19 ± 0.02
56200.21	93.51	LCOGT	r	18.23 ± 0.02
56360.00	237.85	Keck I	r	20.44 ± 0.30
56630.00	481.75	Keck I	r	22.46 ± 0.19

^a Calculated using $\text{MJD}_{r,\text{peak}} = 56096.7$ and $z = 0.107$.

^b The magnitudes have *not* been corrected for Galactic extinction.

supported by a grant AST-1005313 from the National Science Foundation.

The Dark Cosmology Centre is funded by the DNRF. A.G.-Y. is supported by the EU/FP7 via ERC grant No. 307260, the Quantum Universe I-Core program by the Israeli Committee for planning and funding, and the ISF, GIF, Minerva, and ISF grants, WIS-UK “making connections”, and Kimmel and ARCHES awards. Support for D.A.P. was provided by NASA through Hubble Fellowship grant HST-HF-51296.01-A awarded by the Space Telescope Science Institute, which is operated by the

Table 11
Log of observations of iPTF 13dcc.

MJD (days)	Phase ^a (days)	Telescope	Filter	Magnitude ^b AB
56533.36	-59.36	P48	R	19.68 ± 0.12
56533.42	-59.32	P48	R	19.73 ± 0.06
56533.45	-59.29	P48	R	19.76 ± 0.05
56537.35	-56.57	P48	R	19.66 ± 0.06
56537.47	-56.49	P48	R	19.86 ± 0.04
56537.50	-56.46	P48	R	19.70 ± 0.04
56538.45	-55.80	P48	R	19.80 ± 0.04
56539.34	-55.18	P48	R	19.66 ± 0.07
56539.38	-55.15	P48	R	19.79 ± 0.07
56539.42	-55.12	P48	R	19.80 ± 0.06
56540.44	-54.41	P48	R	19.98 ± 0.19
56541.34	-53.78	P48	R	19.73 ± 0.08
56541.37	-53.76	P48	R	19.55 ± 0.17
56541.41	-53.73	P48	R	19.38 ± 0.17
56542.34	-53.08	P48	R	19.77 ± 0.08
56542.45	-53.00	P48	R	19.69 ± 0.06
56542.49	-52.98	P48	R	19.71 ± 0.06
56543.39	-52.35	P48	R	19.84 ± 0.06
56543.46	-52.30	P48	R	19.91 ± 0.06
56543.50	-52.27	P48	R	19.74 ± 0.05
56545.33	-51.00	P48	R	19.55 ± 0.07
56546.32	-50.30	P48	R	19.76 ± 0.08
56546.43	-50.22	P48	R	19.86 ± 0.05
56546.46	-50.20	P48	R	19.86 ± 0.05
56547.37	-49.57	P48	R	19.79 ± 0.07
56547.49	-49.48	P48	R	19.80 ± 0.06
56548.32	-48.90	P48	R	19.82 ± 0.07
56548.47	-48.80	P48	R	19.76 ± 0.04
56548.51	-48.77	P48	R	19.71 ± 0.06
56549.41	-48.14	P48	R	19.88 ± 0.04
56549.45	-48.11	P48	R	19.82 ± 0.04
56549.49	-48.09	P48	R	19.76 ± 0.03
56550.39	-47.45	P48	R	19.77 ± 0.07
56550.48	-47.39	P48	R	19.83 ± 0.04
56550.51	-47.37	P48	R	19.81 ± 0.03
56551.42	-46.74	P48	R	19.78 ± 0.08
56551.46	-46.71	P48	R	19.86 ± 0.07
56551.49	-46.69	P48	R	19.83 ± 0.04
56552.40	-46.06	P48	R	19.76 ± 0.09
56552.44	-46.02	P48	R	19.88 ± 0.08
56552.47	-46.00	P48	R	19.80 ± 0.09
56561.28	-39.84	P48	R	19.81 ± 0.16
56561.36	-39.79	P48	R	19.87 ± 0.10
56561.40	-39.77	P48	R	19.85 ± 0.09
56562.45	-39.03	P48	R	19.90 ± 0.08
56562.48	-39.01	P48	R	19.81 ± 0.07
56562.51	-38.98	P48	R	19.72 ± 0.08
56563.42	-38.35	P48	R	19.74 ± 0.09
56563.49	-38.30	P48	R	19.75 ± 0.08
56563.52	-38.28	P48	R	19.91 ± 0.12
56564.43	-37.65	P48	R	19.80 ± 0.07
56564.48	-37.61	P48	R	19.95 ± 0.07
56564.51	-37.59	P48	R	19.87 ± 0.08
56565.41	-36.96	P48	R	19.78 ± 0.07
56565.47	-36.92	P48	R	19.88 ± 0.06
56565.50	-36.90	P48	R	19.86 ± 0.08
56566.40	-36.27	P48	R	19.82 ± 0.06
56566.45	-36.23	P48	R	19.79 ± 0.05
56566.48	-36.21	P48	R	19.85 ± 0.07
56567.39	-35.58	P48	R	19.77 ± 0.05
56567.44	-35.54	P48	R	19.76 ± 0.06
56567.47	-35.52	P48	R	19.86 ± 0.06
56568.38	-34.89	P48	R	19.93 ± 0.06
56568.45	-34.84	P48	R	19.83 ± 0.07
56568.48	-34.81	P48	R	19.83 ± 0.07
56569.39	-34.18	P48	R	19.77 ± 0.08
56569.46	-34.13	P48	R	19.84 ± 0.06
56569.49	-34.11	P48	R	19.76 ± 0.07
56570.39	-33.48	P48	R	19.83 ± 0.22
56570.47	-33.43	P48	R	19.39 ± 0.16
56570.50	-33.40	P48	R	19.94 ± 0.22
56571.40	-32.77	P48	R	20.01 ± 0.13

^a Calculated using $\text{MJD}_{r,\text{peak}} = 56618.3$ and $z = 0.431$.

^b The magnitudes have *not* been corrected for Galactic extinction.

Table 11
(continued) Log of observations of iPTF 13dcc.

MJD (days)	Phase ^a (days)	Telescope	Filter	Magnitude ^b AB
56571.46	-32.73	P48	R	19.72 ± 0.08
56571.49	-32.71	P48	R	20.08 ± 0.18
56572.39	-32.08	P48	R	19.83 ± 0.08
56572.46	-32.04	P48	R	19.85 ± 0.07
56573.40	-31.38	P48	R	19.83 ± 0.07
56573.44	-31.35	P48	R	19.98 ± 0.07
56573.47	-31.33	P48	R	19.99 ± 0.11
56576.39	-29.29	P48	R	19.83 ± 0.06
56576.49	-29.22	P48	R	19.90 ± 0.08
56576.53	-29.19	P48	R	19.78 ± 0.10
56588.21	-21.03	P48	R	19.76 ± 0.13
56588.35	-20.93	P48	R	20.05 ± 0.16
56588.38	-20.91	P48	R	19.76 ± 0.12
56589.28	-20.28	P48	R	19.62 ± 0.07
56589.31	-20.26	P48	R	19.93 ± 0.10
56589.33	-20.24	P48	R	19.76 ± 0.06
56590.36	-19.53	P48	R	19.74 ± 0.07
56590.38	-19.51	P48	R	19.72 ± 0.08
56591.28	-18.88	P48	R	19.75 ± 0.08
56591.32	-18.85	P48	R	19.64 ± 0.04
56591.35	-18.83	P48	R	19.68 ± 0.04
56592.30	-18.17	P48	R	19.61 ± 0.04
56592.39	-18.11	P48	R	19.67 ± 0.06
56592.42	-18.09	P48	R	19.71 ± 0.04
56596.19	-15.45	P48	R	19.75 ± 0.11
56596.30	-15.37	P48	R	19.66 ± 0.08
56596.33	-15.36	P48	R	19.67 ± 0.07
56597.23	-14.73	P48	R	19.54 ± 0.09
56597.31	-14.67	P48	R	19.70 ± 0.08
56597.34	-14.65	P48	R	19.55 ± 0.07
56598.24	-14.02	P48	R	19.59 ± 0.10
56598.31	-13.97	P48	R	19.62 ± 0.06
56598.33	-13.95	P48	R	19.67 ± 0.07
56599.24	-13.32	P48	R	19.58 ± 0.07
56599.28	-13.29	P48	R	19.71 ± 0.06
56599.30	-13.28	P48	R	19.61 ± 0.06
56600.25	-12.62	P48	R	19.59 ± 0.05
56600.36	-12.54	P48	R	19.54 ± 0.07
56600.39	-12.52	P48	R	19.47 ± 0.16
56602.17	-11.27	P48	R	19.55 ± 0.12
56602.23	-11.23	P48	R	19.57 ± 0.15
56602.25	-11.21	P48	R	19.54 ± 0.11
56603.17	-10.57	P48	R	19.37 ± 0.09
56603.24	-10.53	P48	R	19.44 ± 0.07
56603.29	-10.49	P48	R	19.51 ± 0.06
56604.29	-9.79	P48	R	19.60 ± 0.04
56604.41	-9.71	P48	R	19.57 ± 0.04
56604.44	-9.69	P48	R	19.58 ± 0.06
56605.34	-9.06	P48	R	19.53 ± 0.06
56605.38	-9.03	P48	R	19.62 ± 0.06
56605.41	-9.01	P48	R	19.54 ± 0.05
56607.16	-7.79	P48	R	19.82 ± 0.11
56607.29	-7.69	P48	R	19.54 ± 0.07
56607.32	-7.67	P48	R	19.47 ± 0.07
56608.22	-7.04	P48	R	19.34 ± 0.06
56608.26	-7.02	P48	R	19.60 ± 0.12
56608.29	-6.99	P48	R	19.48 ± 0.10
56609.19	-6.36	P48	R	19.64 ± 0.10
56609.34	-6.26	P48	R	19.45 ± 0.07
56537.33	-56.58	P60	r	19.81 ± 0.04
56637.12	13.15	P60	i	19.95 ± 0.13
56637.12	13.15	P60	r	19.88 ± 0.13
56637.12	13.15	P60	g	20.14 ± 0.11
56645.12	18.74	P60	r	19.93 ± 0.18
56645.12	18.74	P60	g	20.13 ± 0.14
56647.13	20.15	P60	i	19.75 ± 0.16
56647.13	20.15	P60	r	20.83 ± 0.24
56647.14	20.15	P60	g	20.46 ± 0.11
56648.11	20.83	P60	i	20.15 ± 0.10
56648.12	20.84	P60	r	20.02 ± 0.04
56648.12	20.84	P60	g	20.43 ± 0.05
56655.20	25.79	P60	i	19.99 ± 0.12

^a Calculated using $\text{MJD}_{r,\text{peak}} = 56618.3$ and $z = 0.431$.

^b The magnitudes have *not* been corrected for Galactic extinction.

Table 11
(continued) Log of observations of iPTF 13dcc.

MJD (days)	Phase ^a (days)	Telescope	Filter	Magnitude ^b AB
56655.20	25.79	P60	r	20.25 ± 0.11
56655.21	25.79	P60	g	20.85 ± 0.15
56656.17	26.46	P60	i	20.17 ± 0.10
56656.17	26.46	P60	r	20.25 ± 0.08
56656.18	26.47	P60	g	20.66 ± 0.09
56657.13	27.14	P60	i	20.14 ± 0.05
56657.13	27.14	P60	r	20.21 ± 0.03
56657.14	27.14	P60	g	20.62 ± 0.04
56658.13	27.83	P60	i	20.15 ± 0.05
56658.13	27.83	P60	r	20.25 ± 0.04
56658.13	27.84	P60	g	20.66 ± 0.05
56659.20	28.58	P60	i	20.21 ± 0.06
56660.15	29.25	P60	i	20.12 ± 0.06
56660.16	29.25	P60	r	20.29 ± 0.05
56660.16	29.25	P60	g	20.65 ± 0.05
56662.21	30.68	P60	i	20.38 ± 0.13
56662.21	30.68	P60	r	20.30 ± 0.08
56662.22	30.69	P60	g	20.82 ± 0.08
56671.19	36.96	P60	i	20.41 ± 0.15
56671.19	36.96	P60	r	20.60 ± 0.14
56672.19	37.66	P60	i	20.88 ± 0.26
56672.20	37.66	P60	r	20.59 ± 0.21
56673.18	38.35	P60	r	20.60 ± 0.19
56676.13	40.41	P60	i	20.70 ± 0.08
56676.13	40.41	P60	r	21.33 ± 0.10
56676.14	40.42	P60	g	21.59 ± 0.09
56683.25	45.39	P60	i	21.13 ± 0.16
56683.25	45.39	P60	r	21.37 ± 0.19
56685.13	46.70	P60	i	21.41 ± 0.14
56685.13	46.70	P60	r	21.65 ± 0.20
56697.14	55.10	P60	i	21.43 ± 0.21
56697.15	55.10	P60	r	21.51 ± 0.19
56710.18	64.20	P60	i	21.25 ± 0.21
56701.20	57.93	DCT	r	22.20 ± 0.24
56701.20	57.93	DCT	i	21.74 ± 0.21
56908.50	202.79	DCT	r	23.20 ± 0.28
57070.00	315.65	HST	F625W	25.00 ± 0.13

^a Calculated using $\text{MJD}_{r,\text{peak}} = 56618.3$ and $z = 0.431$.

^b The magnitudes have *not* been corrected for Galactic extinction.

Association of Universities for Research in Astronomy, Inc., for NASA, under contract NAS 5-26555. M.S. acknowledges support from EU/FP7-ERC grant 615929. E.O.O. is incumbent of the Arye Dissentshik career development chair and is grateful to support by grants from the Willner Family Leadership Institute Ilan Gluzman (Secaucus NJ), Israel Science Foundation, Minerva, and the I-CORE Program of the Planning and Budgeting Committee and The Israel Science Foundation. Support for I.A. was provided by NASA through the Einstein Fellowship Program, grant PF6-170148. A.V.F.'s supernova group at UC Berkeley is supported through NSF grant AST-1211916, the TABASGO Foundation, and the Christopher R. Redlich Fund. The National Energy Research Scientific Computing Center, which is supported by the Office of Science of the U.S. Department of Energy under Contract No. DE-AC02-05CH11231, provided staff, computational resources, and data storage for this project. Part of this research was carried out at the Jet Propulsion Laboratory, California Institute of Technology, under a contract with the National Aeronautics and Space Administration.

- Ahn, C. P., Alexandroff, R., Allende Prieto, C., et al. 2014, *ApJS*, 211, 17
- Arnett, W. D. 1980, *ApJ*, 237, 541
- . 1982, *ApJ*, 253, 785
- Baklanov, P. V., Sorokina, E. I., & Blinnikov, S. I. 2015, *Astronomy Letters*, 41, 95
- Barbary, K., Dawson, K. S., Tokita, K., et al. 2009, *ApJ*, 690, 1358
- Benetti, S., Nicholl, M., Cappellaro, E., et al. 2014, *MNRAS*, 441, 289
- Blinnikov, S. I., & Sorokina, E. I. 2010, *ArXiv e-prints*, arXiv:1009.4353
- Brown, T. M., Baliber, N., Bianco, F. B., et al. 2013, *PASP*, 125, 1031
- Cardelli, J. A., Clayton, G. C., & Mathis, J. S. 1989, *ApJ*, 345, 245
- Cenko, S. B., Fox, D. B., Moon, D.-S., et al. 2006, *PASP*, 118, 1396
- Chatzopoulos, E., Wheeler, J. C., & Vinko, J. 2012, *ApJ*, 746, 121
- Chatzopoulos, E., Wheeler, J. C., Vinko, J., Horvath, Z. L., & Nagy, A. 2013, *ApJ*, 773, 76
- Chen, T.-W., Smartt, S. J., Yates, R. M., et al. 2016, *ArXiv e-prints*, arXiv:1605.04925
- Chen, T.-W., Smartt, S. J., Jerkstrand, A., et al. 2015, *MNRAS*, 452, 1567
- Chevalier, R. A. 1982, *ApJ*, 258, 790
- Chevalier, R. A., & Fransson, C. 1994, *ApJ*, 420, 268
- Chevalier, R. A., & Irwin, C. M. 2011, *ApJ*, 729, L6
- Chugai, N. N., & Danziger, I. J. 1994, *MNRAS*, 268, 173
- Dessart, L., Hillier, D. J., Waldman, R., Livne, E., & Blondin, S. 2012, *MNRAS*, 426, L76
- Dessart, L., Waldman, R., Livne, E., Hillier, D. J., & Blondin, S. 2013, *MNRAS*, 428, 3227
- Dexter, J., & Kasen, D. 2013, *ApJ*, 772, 30
- Drake, A. J., Djorgovski, S. G., Mahabal, A., et al. 2009, *ApJ*, 696, 870
- Drake, A. J., Djorgovski, S. G., Mahabal, A. A., et al. 2013, *The Astronomer's Telegram*, 5437, 1
- Filippenko, A. V. 1997, *ARA&A*, 35, 309
- Firth, R. E., Sullivan, M., Gal-Yam, A., et al. 2015, *MNRAS*, 446, 3895
- Gal-Yam, A. 2012, *Science*, 337, 927
- Gal-Yam, A., Mazzali, P., Ofek, E. O., et al. 2009, *Nature*, 462, 624
- Gehrels, N., Chincarini, G., Giommi, P., et al. 2004, *ApJ*, 611, 1005
- Hogg, D. W., Baldry, I. K., Blanton, M. R., & Eisenstein, D. J. 2002, *ArXiv Astrophysics e-prints*, arXiv:astro-ph/0210394
- Hogg, D. W., Blanton, M., Lang, D., Mierle, K., & Roweis, S. 2008, in *Astronomical Society of the Pacific Conference Series*, Vol. 394, *Astronomical Data Analysis Software and Systems XVII*, ed. R. W. Argyle, P. S. Bunclark, & J. R. Lewis, 27
- Howell, D. A., Kasen, D., Lidman, C., et al. 2013, *ApJ*, 779, 98
- Insera, C., Smartt, S. J., Jerkstrand, A., et al. 2013, *ApJ*, 770, 128
- Insera, C., Smartt, S. J., Gall, E. E. E., et al. 2016, *ArXiv e-prints*, arXiv:1604.01226
- Japelj, J., Vergani, S. D., Salvaterra, R., Hunt, L. K., & Mannucci, F. 2016, *A&A*, 593, A115
- Jerkstrand, A., Smartt, S. J., & Heger, A. 2016, *MNRAS*, 455, 3207
- Kasen, D., & Bildsten, L. 2010, *ApJ*, 717, 245
- Kasen, D., Metzger, B. D., & Bildsten, L. 2016, *ApJ*, 821, 36
- Kasen, D., & Woosley, S. E. 2007, *ApJ*, 656, 661
- Laher, R. R., Surace, J., Grillmair, C. J., et al. 2014, *PASP*, 126, 674
- Law, N. M., Kulkarni, S. R., Dekany, R. G., et al. 2009, *PASP*, 121, 1395
- Leloudas, G., Chatzopoulos, E., Dilday, B., et al. 2012, *A&A*, 541, A129
- Leloudas, G., Schulze, S., Krühler, T., et al. 2015, *MNRAS*, 449, 917
- Lunnan, R., Chornock, R., Berger, E., et al. 2014, *ApJ*, 787, 138
- . 2015, *ApJ*, 804, 90
- Markwardt, C. B. 2009, in *Astronomical Society of the Pacific Conference Series*, Vol. 411, *Astronomical Data Analysis Software and Systems XVIII*, ed. D. A. Bohlender, D. Durand, & P. Dowler, 251
- Mazzali, P. A., Sullivan, M., Pian, E., Greiner, J., & Kann, D. A. 2016, *MNRAS*, 458, 3455
- Miller, J. S., & Stone, R. P. S. 1993, *Lick Obs. Tech. Rep.* 66 (Univ. California, Santa Cruz)
- Moré, J. J. 1978, in *Numerical Analysis*, ed. G. A. Watson, Vol. 630 (Springer-Verlag: Berlin), 105
- Moriya, T., Tominaga, N., Tanaka, M., Maeda, K., & Nomoto, K. 2010, *ApJ*, 717, L83
- Moriya, T. J., Blinnikov, S. I., Tominaga, N., et al. 2013, *MNRAS*, 428, 1020
- Moriya, T. J., Liu, Z.-W., Mackey, J., Chen, T.-W., & Langer, N. 2015, *A&A*, 584, L5
- Moriya, T. J., & Maeda, K. 2012, *ApJ*, 756, L22
- Moriya, T. J., & Tominaga, N. 2012, *ApJ*, 747, 118
- Nakar, E., & Piro, A. L. 2014, *ApJ*, 788, 193
- Neill, J. D., Sullivan, M., Gal-Yam, A., et al. 2011, *ApJ*, 727, 15
- Nicholl, M., & Smartt, S. J. 2016, *MNRAS*, 457, L79
- Nicholl, M., Smartt, S. J., Jerkstrand, A., et al. 2013, *Nature*, 502, 346
- . 2015, *ApJ*, 807, L18
- Nicholl, M., Berger, E., Smartt, S. J., et al. 2016, *ApJ*, 826, 39
- Ofek, E. O., Cameron, P. B., Kasliwal, M. M., et al. 2007, *ApJ*, 659, L13
- Ofek, E. O., Laher, R., Law, N., et al. 2012, *PASP*, 124, 62
- Ofek, E. O., Arcavi, I., Tal, D., et al. 2014, *ApJ*, 788, 154
- Oke, J. B., & Gunn, J. E. 1983, *ApJ*, 266, 713
- Oke, J. B., Cohen, J. G., Carr, M., et al. 1995, *PASP*, 107, 375
- Pastorello, A., Smartt, S. J., Botticella, M. T., et al. 2010, *ApJ*, 724, L16
- Perley, D. A., Quimby, R. M., Yan, L., et al. 2016, *ApJ*, 830, 13
- Pinto, P. A., & Eastman, R. G. 2000, *ApJ*, 530, 757
- Piro, A. L. 2015, *ApJ*, 808, L51
- Planck Collaboration, Ade, P. A. R., Aghanim, N., et al. 2016, *A&A*, 594, A13
- Quimby, R. M., Kulkarni, S. R., Kasliwal, M. M., et al. 2011, *Nature*, 474, 487
- Quimby, R. M., Arcavi, I., Sternberg, A., et al. 2012, *The Astronomer's Telegram*, 4121, 1
- Rabinak, I., & Waxman, E. 2011, *ApJ*, 728, 63
- Rahmer, G., Smith, R., Velur, V., et al. 2008, in *Society of Photo-Optical Instrumentation Engineers (SPIE) Conference Series*, Vol. 7014, *Society of Photo-Optical Instrumentation Engineers (SPIE) Conference Series*
- Rau, A., Kulkarni, S. R., Law, N. M., et al. 2009, *PASP*, 121, 1334
- Sapir, N., & Waxman, E. 2016, *ArXiv e-prints*, arXiv:1607.03700
- Schlaflly, E. F., & Finkbeiner, D. P. 2011, *ApJ*, 737, 103
- Smith, M., Sullivan, M., D'Andrea, C. B., et al. 2016, *ApJ*, 818, L8
- Smith, N., Li, W., Foley, R. J., et al. 2007, *ApJ*, 666, 1116
- Sorokina, E., Blinnikov, S., Nomoto, K., Quimby, R., & Tolstov, A. 2016, *ApJ*, 829, 17
- Taddia, F., Fremling, C., Sollerman, J., et al. 2016, *A&A*, 592, A89
- Thône, C. C., de Ugarte Postigo, A., García-Benito, R., et al. 2015, *MNRAS*, 451, L65
- Valenti, S., Howell, D. A., Stritzinger, M. D., et al. 2016, *MNRAS*, 459, 3939
- Vreeswijk, P. M., Savaglio, S., Gal-Yam, A., et al. 2014, *ApJ*, 797, 24
- Wang, S. Q., Liu, L. D., Dai, Z. G., Wang, L. J., & Wu, X. F. 2016, *ApJ*, 828, 87
- Wang, S. Q., Wang, L. J., Dai, Z. G., & Wu, X. F. 2015, *ApJ*, 799, 107
- Wheeler, J. C., Johnson, V., & Clocchiatti, A. 2015, *MNRAS*, 450, 1295
- Woosley, S. E. 2010, *ApJ*, 719, L204
- Yan, L., Quimby, R., Ofek, E., et al. 2015, *ApJ*, 814, 108
- Yaron, O., & Gal-Yam, A. 2012, *PASP*, 124, 668
- Young, D. R., Smartt, S. J., Valenti, S., et al. 2010, *A&A*, 512, A70
- Zacharias, N., Monet, D. G., Levine, S. E., et al. 2004, in *Bulletin of the American Astronomical Society*, Vol. 36, *American Astronomical Society Meeting Abstracts*, 1418